Hindawi
Structural Control and Health Monitoring
Volume 2023, Article ID 9770996, 25 pages
https://doi.org/10.1155/2023/9770996

Research Article

Development and Experimental Verification of an Intelligent Isolation System Based on Long Short-Term Memory Module Model for Ground Motion Characteristics Prediction

Tzu-Kang Lin,[1] **Lyan-Ywan Lu**,[2] **Chun-Kai Chuang**,[1] **and Ting-Kuan Lin**[1]

[1]*Department of Civil Engineering, National Yang Ming Chiao Tung University, Hsinchu 30010, Taiwan*
[2]*Department of Civil Engineering, National Cheng Kung University, Tainan 701, Taiwan*

Correspondence should be addressed to Lyan-Ywan Lu; lylu@mail.ncku.edu.tw

Received 18 November 2022; Revised 23 April 2023; Accepted 26 April 2023; Published 10 May 2023

Academic Editor: Lucia Faravelli

Semiactive seismic control requires appropriate control laws that dictate the behavior of seismic suppression devices based on measurements and feedback during an earthquake. Optimal control parameters should be determined in real time to achieve high performance. The initial ground motion characteristics of an earthquake substantially affect control performance. In this study, a genetic algorithm (GA)-optimized long short-term memory (LSTM)-based intelligent control system (hereafter denoted GA-LSTM system) for obtaining optimal control parameters for a semiactive variable-stiffness isolation system was proposed. First, the LSTM module classifies earthquakes as near-fault or far-field events to determine the optimal control strategy. Second, earthquakes from a global database are analyzed to determine a fuzzy inference surface for the optimal parameters of the earthquake suppression system. Both numerical simulations and shaking table experimental results indicated that the proposed GA-LSTM system exhibited superior isolation displacement and superstructure acceleration suppression for both near-fault and far-field earthquakes when compared with other control techniques. The proposed intelligent control system is highly efficient and could reliably protect structures from earthquakes with any ground motion characteristics.

1. Introduction

Countries located at tectonic plate junctions and seismic belts experience thousands of earthquakes annually. Such earthquakes threaten their economies and human life. Numerous researchers have studied earthquake disaster prevention techniques, including seismic design codes, structural reinforcement systems, and postdisaster rehabilitation strategies, to reduce the adverse impacts of earthquakes. Earthquake early warning systems (EEWS) have been developed in numerous countries in recent years. The EEWS concept was first proposed by Nakamura et al. in 1988, who applied it to Japanese railways [1]. They proposed implementing two-stage alarms that can indicate the arrival of P- and S-waves and thus stop trains, reducing damage. EEWSs have now been implemented in various industrial fields. To establish an EEWS, a robust earthquake monitoring network must first be developed. Bakun et al. and Espinosa-Arandaet al. designed EEWSs in the United States and Mexico, respectively, by arranging numerous seismographs that receive signals and transmit them to remote areas to increase the time for disaster prevention [2, 3].

Structural control is among the most efficient seismic protection technologies for structures or equipment and can be realized in three different forms: passive, active, and semiactive control. Each of these control methods has its own unique characteristics, advantages, and limitations. Passive control involves the use of materials and devices that absorb or dissipate seismic energy without requiring external power input. In 1976, the application of seismic isolation was utilized in Somplago Viaduct of the Udine-Tarvisio freeway. By comprising sliding devices on the piers and the rubber bumpers between the deck and the abutment, the structure

successfully survived under several violent earthquakes [4]. In 1999, Shape Memory Alloy Devices (SMAD) were proposed by Castellano et al. [5]. The innovative technique for restoring cultural heritage structure improves the seismic resistance by prestressing the structure while not overstressing it through the alloy's superelastic properties. In 2000, SMAD was placed within the insertion of vertical post-tensioned tie bars to increase the bending resistance and to restore the damaged masonry bell tower in Italy [6, 7]. In 2010, Ozbulut and Hurlebaus proposed a passive control method for protecting bridges by including an isolation device constructed from a nickel-titanium memory alloy between bridge columns and decks [8]; numerical simulations revealed that this device reduced bridge deck displacement during earthquakes by approximately 50% compared with the original isolation equipment. In addition, studies have proposed passive friction control systems [9–12] in which structural responses are reduced by driving friction impedance between structural elements and passive control devices during an earthquake. In 2019, Clemente et al. proposed a seismic isolation system made of High Damping Rubber Bearings (HDRB), and analysis of the actual behaviors of the HDRB system was conducted under low energy earthquakes [13]. Passive control typically involves the installation of dampers or energy dissipation devices, and the effectiveness depends on the characteristics of the structure, including its mass, stiffness and damping ratio. By properly designing the system, a passive antiseismic system with energy dissipation device can protect the structure when subjected to either a far-field earthquake or a near-fault earthquake. As a result, infrastructures such buildings, bridges, and viaducts will not be damaged under violent earthquakes [14]. Active control devices, such as active tuned mass dampers, active tendons, or active bracings, are often used to mitigate the vibration of tall buildings caused by strong winds. The total energy of the controlled structure is typically minimized using an optimization method such as linear–quadratic–Gaussian (LQG) control [15]. However, these control methods often have high energy requirements, and earthquakes often destabilize power supply systems; thus, these systems are vulnerable to power failures. Passive and active control methods can be integrated to derive semiactive control methods, which typically have greater stability and performance than either method alone. Hence, semiactive systems are widely used for structural control. For example, in 2000, Tritchkov et al. proposed a retractable sliding device [16] that is isolated by a mechanical link with a two-branch elastic force-displacement response. In 2005, Narasimhan and Nagarajaiah proposed a semiactive independent variable-stiffness (SAIVS) system [17] in which an actuator is used to change the angle of four diamond-shaped springs to adjust the system's stiffness, improving its performance. Semiactive control requires efficiency; thus, Lu et al. [18] proposed a least-input-energy control law for a variable-stiffness semiactive isolation system with a leverage mechanism.

Recent improvements in computing power have enabled the rapid development and implementation of artificial intelligence techniques such as neural networks. The recurrent neural network (RNN) architecture was first proposed by Rumelhart et al. [19]. Unlike feed-forward neural networks, which map inputs directly to specific outputs, RNNs recursively backpropagate errors to update weight values during training and are thus typically more suitable for processing time-series data [20]. In 1997, Hochreiter and Schmidhuber proposed an RNN with a constant error carousel, denoted the long short-term memory (LSTM) model, to solve the vanishing gradient problem [21]. In 2001, Kolen and Kremer indicated that conventional RNNs are often unsuitable for handling tasks with long time lags. RNNs can learn from only data with time lags of up to 10 steps between relevant input events [22]; however, LSTM can bridge large time legs of 1000 steps or more. LSTM has been applied for handwriting recognition [23] and even for speech recognition in Google Voice in 2015. In 2019, Pawar et al. applied an LSTM model to nonlinear stock market dynamics [24], and in 2020, Apaydin et al. used the architecture for the challenging task of accurately estimating river flows [25].

Conventionally, the classification of near-fault and far-field earthquakes was often performed using the method proposed by Newmark et al. [26] on the basis of the ratio of the measured vertical and horizontal acceleration. Subsequently, scholars have found that the superposition of S-waves along the rupture direction causes energy to accumulate in this direction; especially for those stations adjacent to the fault area [27–29]. The ground motion velocity often has pulses due to this energy accumulation. Numerous studies have applied various analytical methods to earthquake data to determine ground motion characteristics; such methods include wavelet analysis for near-fault ground motion classification [27] and seismic hazard analysis based on an empirically calibrated framework or a probabilistic framework [29] for assessing near-fault earthquakes characteristics. Compared with those generated by far-field earthquakes, signals generated by near-fault earthquakes have higher acceleration, velocity, and displacement peaks. Moreover, velocity pulses can often be observed in the time history of near-fault earthquake owing to the directional nature of fault ruptures, permanent surface displacement, earthquake magnitude, and other phenomena [30]. Because these pulses cause structures to undergo rapid cyclic motion and thus receive greater energy within a shorter period, near-fault earthquakes often engender greater structural damage than far-field earthquakes do.

In this study, an efficient genetic algorithm (GA)-optimized LSTM control system (hereafter, denoted GA-LSTM system) for obtaining optimal control parameters for a semiactive leverage-type stiffness-controllable isolation system (LSCIS) was developed [31]. The proposed intelligent isolation system was designed following the performance-based control strategy for precious vibration-sensitive devices such as cabinets in high-tech factories or precision instruments in hospital. A flowchart of the system development process is presented in Figure 1. A previously developed GA-based fuzzy controller did not perform well since it could not effectively classify near-fault and far-field earthquakes. Accordingly, the goal of the present study was to extend this controller by incorporating an LSTM-based

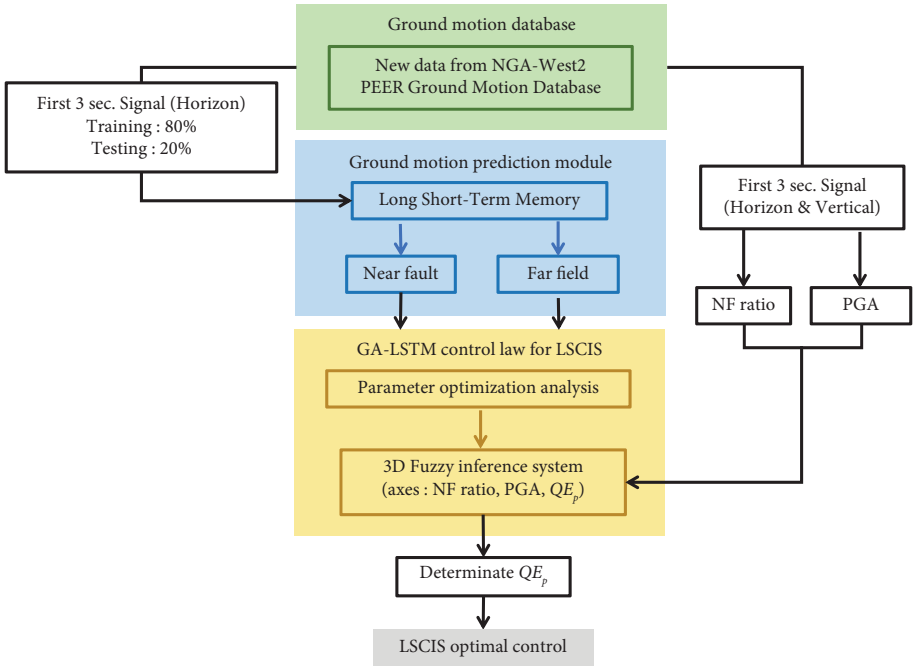

Figure 1: Flowchart of the GA-LSTM control system.

prediction module. Moreover, the fuzzy inference surface of the GA-based fuzzy controller was further enhanced by selecting representative earthquakes from a world-wide database and classifying them as sensitive and insensitive to control parameters. Finally, simulations and experiments were performed to verify the performance of the proposed GA-LSTM system. The rest of this paper is organized as follows. In Section 2, the seismic database and the establishment of the LSTM prediction model are presented. In Section 3, the numerical analysis model and formula for determining the optimal stiffness of the LSCIS isolation layer are described. In Section 4, the derivation and fuzzification of the potential energy weight parameter QE_p in the GA-LSTM control law are presented. The fuzzy surface of the control parameters based on near-fault/far-field (NF) ratio, which is a parameter to define the near-fault property of the earthquakes, and the predicted PGA is established to optimize the control performance. In Sections 5 and 6, comparisons of the control performance of the proposed GA-LSTM system with that of conventional methods through the use of both numerical simulations and a shaking table experiment are provided. Finally, in Section 7, a summary of the results and the conclusions are presented.

2. LSTM Prediction Module

2.1. Data Preprocessing. In this study, the LSTM model proposed by Hochreiter and Schmidhuber in 1997 [32] was modified and used to establish an earthquake ground motion prediction module. An RNN was applied to classify the recorded ground motion time-series data to determine appropriate control parameters before the mainshock. Ground motion data provided by the Next Generation Attenuation of Ground Motions Project, completed by the Pacific Earthquake Engineering Research Center (PEER) were collected [33]. The near-fault database was selected from the seismic database compiled by Shahi and Baker in 2014 [34], which is according to the NGA project of PEER. The earthquake data with the epicentral distance of more than 15 kilometers was deleted to avoid some earthquakes with velocity pulses but low intensity, which cannot cause large displacements to the isolation layer. The far-field earthquake database screens PEER seismic data other than those written by Shahi and Baker [34], and the epicenter must be 20 to 40 kilometers away. This method is to make the seismic data have the difference between near-fault and far-field. The earthquake arrival time is typically determined using the short-term average (STA) and long-term average (LTA) criterion (hereafter STA/LTA ratio) for the vertical acceleration signals of P-waves, which arrive earlier than the mainshock during an earthquake, as shown in Figure 2. STA is the average value of the acceleration signal over 1 second before the current time step, and LTA is the average value of the acceleration signal over 10 seconds before the current time step. Based on the previous research [35], the value of STA/LTA can be treated as an indicator to determine the triggering time of an earthquake in the control system. If the STA/LTA value exceeds a preset threshold, the ground motion data will be recorded as an earthquake event until the recession of the STA/LTA value. In the end, the database was used to collect 1652 earthquake data, including 754 near-fault earthquakes, and 898 far-field earthquakes.

In this study, the first 3 seconds of the horizontal acceleration record were preprocessed and used as the input to the LSTM module. To standardize the earthquake records acquired from various databases in the world, the sampling frequency of all records was unified to 50 Hz, and the number of 3 s time-series was set to 151.

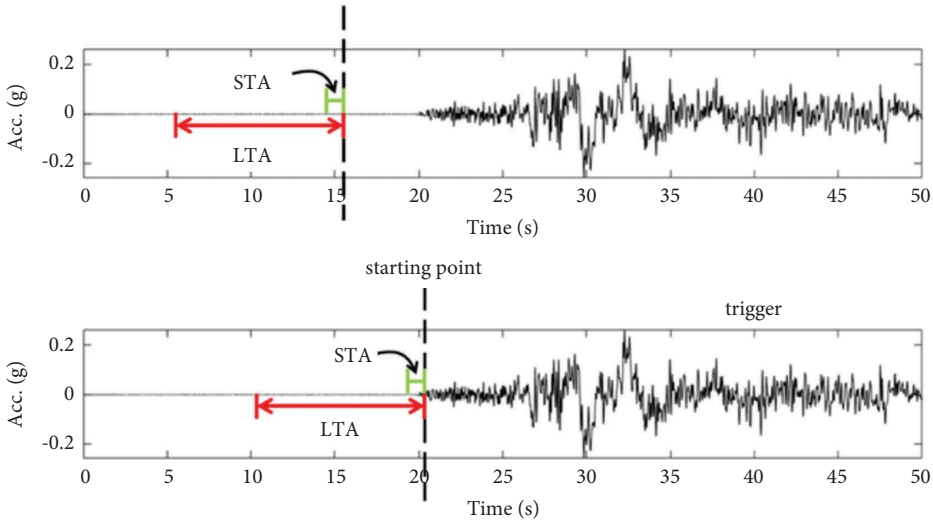

Figure 2: STA/LTA triggering criterion for vertical acceleration signal.

Furthermore, the amplitude of the 3 s horizontal acceleration record was discretized into 402 intervals of 0.005 cm/s^2, as shown in Figure 3(a) to enhance the contrast between points in the time history. To reduce the effects of outlier data, amplitudes of 0 cm/s^2 were assigned to the interval 200, and those less than −1000 cm/s^2 or greater than 1000 cm/s^2 were assigned to the intervals 0 and 401, respectively. The output time history is displayed in Figure 3(b) and was determined to be an effective discretization of the data in that it could retain the characteristics, amplitudes, and phases of the original earthquake waves.

2.2. LSTM Module. The LSTM module is structured with an input data length of 151 and an embedding layer at the beginning to reduce the dimension of the training data from 402 to 10, as shown in Table 1. The LSTM module has 10 neurons, and all of the input and past output values are connected to the neurons in the LSTM memory cell. The module includes two hidden layers with 80 and 20 neurons; the Rectified Linear Unit (ReLU) function serves as the excitation function in both layers of the AI network. Finally, because the LSTM module was designed for predicting ground motion characteristics, the output layer scale was set to 1 in this study, with a binary sigmoid function serving as its excitation function. Each layer includes a dropout layer to avoid excessive dependencies between neurons that could cause overfitting. A binary cross-entropy loss function was selected as the loss function in this study. Approximately 80% of the input data were randomly selected as training samples; the remaining 20% were used for testing. Each sample comprised 151 data points and was labeled as 1 for a near-fault earthquake or 0 for a far-field earthquake. Earthquakes were classified as near-fault if the network output was greater than or equal to 0.5 and as far-field otherwise.

The training results are displayed in Figure 4; by the 80th training generation, both the accuracy and error curves had gradually converged. The confusion matrix for the test dataset is presented in Figure 4(c). The accuracy of the LSTM module in distinguishing near-fault and far-field earthquakes was determined to be approximately 94%. These results thus indicate that the LSTM module can classify an earthquake only 3 s after receiving an earthquake signal, and this module is likely to be effective for use in an intelligent control mechanism. On the basis of the ground motion characteristics, the optimal control parameters can be adjusted for different control objectives.

3. LSCIS and Control Law

3.1. LSCIS Analytical Models. As mentioned, the intelligent GA-LSTM system was proposed for controlling the LSCIS [31]. Mathematical and physical models of the LSCIS are presented in Figures 5 and 6, respectively. A lever connects the isolation layer and a spring of constant stiffness (Figure 6); the length ratio of the lever arm can be altered by moving the pivot position. In Figures 5 and 6, m_s represent the mass of the superstructure; m_b represents the mass of the isolation layer; c_s represents the damping coefficient of the superstructure; k_s represents the stiffness of the superstructure; $x_p(t)$ represents the pivot displacement; $\ddot{x}_g(t)$ represents the ground acceleration; and $x_s(t)$ and $x_b(t)$ represent the relative-to-the-ground displacement of the superstructure and isolation layer, respectively. In Figure 5, k_{r0} denotes the initial isolation stiffness when the pivot is at the center of the lever arm (i.e., when $x_p = 0$). $\Delta k_r(t)$ is the increment or decrement of the isolation stiffness due to the pivot displacement $x_p(t)$.

The relationship between the stiffness increment $\Delta k_r[n]$ and the pivot displacement $x_p[n]$ of the isolation layer at time step n can be derived as follows [31]:

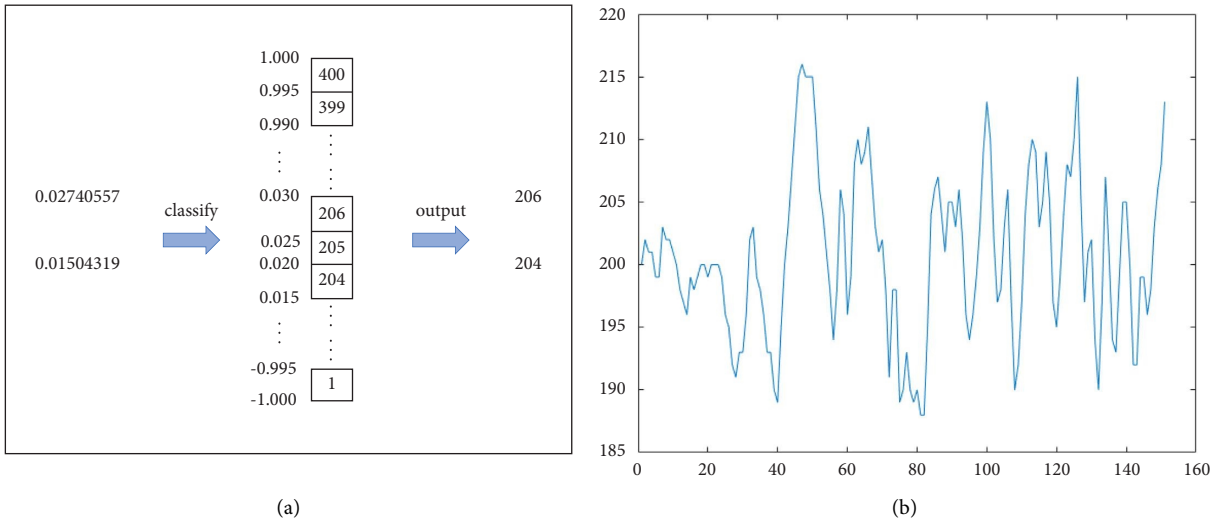

(a) (b)

Figure 3: Preprocessing of the database for LSTM module. (a) Intervalization process. (b) Time history of a discretized earthquake.

Table 1: Structure of LSTM module.

Model: "sequential_1"		
Layer (type)	Output shape	Number of parameters
embedding_1 (embedding)	(None, 151, 10)	4020
dropout_1 (dropout)	(None, 151, 10)	0
lstm_1 (LSTM)	(None, 10)	840
dense_1 (dense)	(None, 80)	880
dropout_2 (dropout)	(None, 80)	0
dense_2 (dense)	(None, 20)	1620
dropout_3 (dropout)	(None, 20)	0
dense_3 (dense)	(None, 1)	21
Total number of parameters: 7381		
Total number of trainable parameters: 7381		
Total number of nontrainable parameters: 0		

$$\Delta k_r[n] = \left[\frac{2Lx_p[n]}{0.5L - x_p[n]^2}\right]k_{r0}, \tag{1}$$

where L is the total length of the lever. This equation indicates that the stiffness increment $\Delta k_r[n]$ of the LSCIS can be controlled in real time by changing the position of the leverage pivot point. Conversely, if the desired stiffness increment $\Delta k_r[n]$ is determined by a control law, the pivot position to achieve this increment can be computed by solving equation (1) as follows:

$$x_p[n] = \frac{L\left(k_{r0} + 0.5\Delta k_r[n] - \sqrt{{k_{r0}}^2 + k_{r0}\Delta k_r[n]}\right)}{\Delta k_r[n]}, \tag{2}$$

In this study, for practical reason, the range of the pivot point $x_p[n]$ was assumed to be between $0.5L$ and $-0.5L$, and the corresponding range of the stiffness increment $\Delta k_r(t)$ was assumed to be between $-0.8k_{r0}$ and $0.5k_{r0}$.

The dynamic equation of the LSCIS can be expressed using the following state-space equation derived from the Lagrange equation [18]:

$$\dot{\mathbf{z}}(t) = \mathbf{A}\mathbf{z}(t) + \mathbf{B}\left(\Delta u_r(t) + u_f(\mathrm{t})\right) + \mathbf{E}\ddot{x}_g(t), \tag{3}$$

where $\mathbf{z}(t)$ denotes the state vector, $\mathbf{A}$ denotes the system matrix, $\mathbf{B}$ denotes the isolation force matrix, and $\mathbf{E}$ denotes the seismic disturbance matrix. $\Delta u_r[n]$ and $u_f(\mathrm{t})$ are the restoring force increment and friction force of the isolation layer, respectively. Details of matrices $\mathbf{z}(t)$, $\mathbf{A}$, $\mathbf{B}$, and $\mathbf{E}$ are provided as follows:

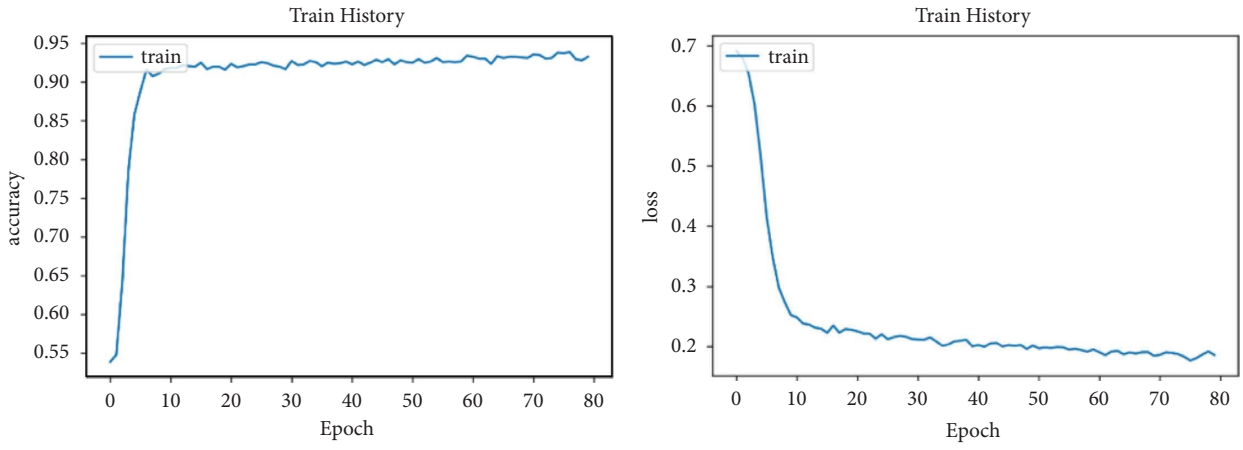

Confusion Matrix		Actual Value	
		Near	Not Near
Predicted Value	Near	134	8
	Not Near	11	179

(c)

Figure 4: Training and testing results of the LSTM module. (a) Accuracy convergence curve. (b) Error convergence curve. (c) Confusion matrix of testing results.

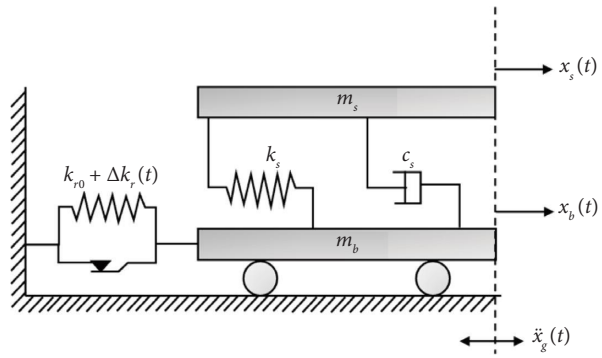

Figure 5: Numerical model of the LSCIS.

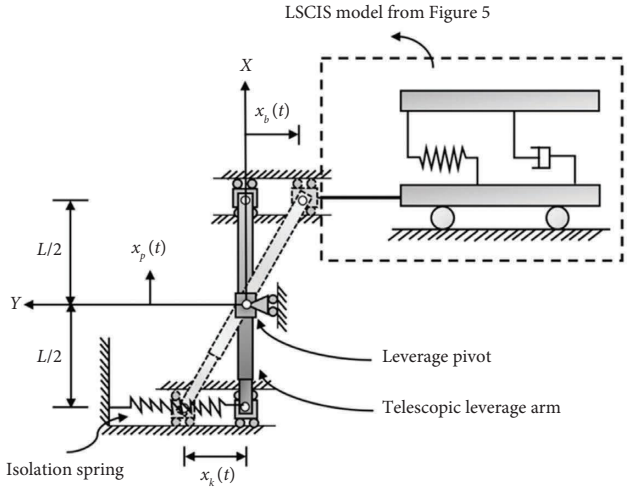

Figure 6: Physical model of the LSCIS.

$$\mathbf{A} = \begin{bmatrix} -\mathbf{M}^{-1}\mathbf{C} & -\mathbf{M}^{-1}\mathbf{K} \\ \mathbf{I} & \mathbf{0} \end{bmatrix},$$

$$\mathbf{z}(t) = \begin{Bmatrix} \dot{x}_s(t) \\ \dot{x}_b(t) \\ x_s(t) \\ x_b(t) \end{Bmatrix},$$

$$\mathbf{B} = \begin{Bmatrix} 0 \\ -1/m_b \\ 0 \\ 0 \end{Bmatrix},$$

$$\mathbf{E} = \begin{Bmatrix} -1 \\ -1 \\ 0 \\ 0 \end{Bmatrix}, \quad (4)$$

$$\mathbf{M} = \begin{bmatrix} m_s & 0 \\ 0 & m_b \end{bmatrix},$$

$$\mathbf{K} = \begin{bmatrix} k_s & -k_s \\ -k_s & k_s + k_{r0} \end{bmatrix},$$

$$\mathbf{C} = \begin{bmatrix} c_s & -c_s \\ -c_s & c_s \end{bmatrix},$$

where **M**, **K**, and **C** are the structural mass, stiffness, and damping matrices, respectively. In this study, the force term in each time step Δt was assumed to be constant; the discrete-time solution of equation (3) could then be obtained as follows:

$$\mathbf{z}[n+1] = \mathbf{A}_d\mathbf{z}[n] + \mathbf{B}_d\left(\Delta u_r[n] + u_f[n]\right) + \mathbf{E}_d\ddot{x}_g[n], \quad (5)$$

$$\begin{aligned} \mathbf{A}_d &= e^{\mathbf{A}\Delta t}, \\ \mathbf{B}_d &= \mathbf{A}^{-1}\left(\mathbf{A}_d - \mathbf{I}\right)\mathbf{B}, \\ \mathbf{E}_d &= \mathbf{A}^{-1}\left(\mathbf{A}_d - \mathbf{I}\right)\mathbf{E}, \end{aligned} \quad (6)$$

where $\mathbf{A}_d$, $\mathbf{B}_d$, and $\mathbf{E}_d$ are the discrete-time matrices. $\mathbf{z}[n+1]$ is the discrete-time state vector at time step $n+1$. According to equation (5), the restoring force increment $\Delta u_r[n]$ is related to the stiffness increment $\Delta k_r[n]$ and can be expressed as follows:

$$\begin{aligned} \Delta u_r[n] &= \Delta k_r[n] x_b[n] = \Delta k_r[n]\mathbf{D}_d\mathbf{z}[n], \\ \mathbf{D}_d &= \begin{bmatrix} 0 & 0 & 0 & 1 \end{bmatrix}. \end{aligned} \quad (7)$$

The value of $u_f[n]$ in (5) can be calculated by using the shear balance method [18, 31] as follows:

$$u_f[n] = \min\left(\left|\tilde{u}_f[n]\right|, u_{f,\max}\right)\mathrm{sgn}\left(\tilde{u}_f[n]\right), \quad (8)$$

$$u_{f,\max} = \mu M g, \quad (9)$$

$$\tilde{u}_f[n] = -\left(\mathbf{D}_v\mathbf{B}_d\right)^{-1}\mathbf{D}_v\left(\mathbf{A}_d\mathbf{z}[n] + \mathbf{B}_d\Delta u_r[n] + \mathbf{E}_d\ddot{x}_g[n]\right), \quad (10)$$

$$\mathbf{D}_v = \begin{bmatrix} 0 & 1 & 0 & 0 \end{bmatrix}, \quad (11)$$

where μ denotes the friction coefficient of the isolation layer; M denotes the total weight of the LSCIS, including the superstructure ($M = m_s + m_b$); g denotes gravitational acceleration; $\tilde{u}_f[n]$ denotes the hypothetical friction force obtained with the isolation layer in the sticking state; $\mathrm{sgn}(\tilde{u}_f[n])$ denotes the positive or negative sign of $\tilde{u}_f[n]$; and $\mathbf{D}_v$ denotes the configuration matrix of the support velocity term. According to equations (8)–(10), the frictional force $u_f[n]$ for each step can be determined, and the state vector $\mathbf{z}[n+1]$ can be further derived using equation (5).

3.2. Determination of the Optimal Value for $\Delta\mathbf{k_r}[\mathbf{n}]$. The optimal stiffness increment $\Delta k_r[n]$ was determined using a control law called feed-forward predictive earthquake energy analysis (FPEEA) [36]. In FPEEA, the optimal stiffness increment $\Delta k_r[n]$ is calculated by minimizing the energy efficiency index of the system, which includes the system kinetic energy and potential energy. The main concepts of the FPEEA control method are briefly described as follows.

To determine the optimal $\Delta k_r[n]$, the energy efficiency indicator $J[n+1]$ can be set as follows:

$$J[n+1] = E_k[n+1] + \frac{R}{2}\Delta k_r[n]^2 + QE_p\left(E_{p,\text{sup}}[n+1] + E_{p,\text{iso}}[n+1]\right), \tag{12}$$

where $E_k[n+1]$ is the total kinetic energy of the LSCIS; R is the weighting factor for the control force ($R \geq 0$); $E_{p,\text{sup}}[n+1]$ and $E_{p,\text{iso}}[n+1]$ are the potential energy of the superstructure and the isolation layer at time step $n+1$, respectively; and QE_p is the weighting factor for potential energy. The second term ($(R/2)\Delta k_r[n]^2$) in (12) is included to avoid excessive changes in both stiffness increments $\Delta k_r[n]$ and the LSCIS leverage pivot. Furthermore, the system kinetic energy $E_k[n+1]$ in equation (12) can be expressed as follows:

$$\begin{aligned} E_k[n+1] &= \frac{1}{2}\mathbf{z}[n+1]^T\mathbf{D}_2{}^T\mathbf{M}\mathbf{D}_2\mathbf{z}[n+1] + \mathbf{D}\mathbf{M}\mathbf{D}_2\mathbf{z}[n+1]\dot{x}_g[k] + \frac{1}{2}\mathbf{D}\mathbf{M}\mathbf{D}^{\mathrm{T}}\left(\dot{x}_g[n]\right)^2, \\ \mathbf{D} &= \begin{bmatrix} 1 & 1 \end{bmatrix}, \\ \mathbf{D}_2 &= \begin{bmatrix} 1 & 0 & 0 & 0 \\ 0 & 1 & 0 & 0 \end{bmatrix}, \end{aligned} \tag{13}$$

where $\dot{x}_g[n]$ is the ground velocity.

Because the sampling interval is usually extremely small, the ground velocities at step $n+1$ and step n can be assumed to be identical ($\dot{x}_g[k+1] \approx \dot{x}_g[k]$), simplifying the control calculations. Subsequently, to minimize the energy index $J[n+1]$ and solve for the optimal stiffness increment $\Delta k_{r,\text{opt}}[n]$, the energy index in equation (11) can be differentiated with respect to the variable $\Delta k_r[n]$ and set to zero as follows:

$$\frac{d(J[n+1])}{d(\Delta k_r[n])} = 0. \tag{14}$$

Substituting equations (12) into (14) the optimal stiffness increment $\Delta k_{r,\text{opt}}[n]$ can be determined as follows:

$$\Delta k_{r,\text{opt}}[n] = \frac{-\left(a_2[n] + QE_p \times b_{3,\text{sup}} + QE_p \times b_{3,\text{iso}}[n]\right)}{a_1[n] + R + QE_p \times b_{2,\text{sup}}[n] + QE_p \times b_{2,\text{iso}}[n]}, \tag{15}$$

where the coefficients $a_1[n]$, $a_2[n]$, $b_{2,\text{iso}}[n]$, $b_{2,\text{sup}}[n]$, $b_{3,\text{iso}}[n]$, and $b_{3,\text{sup}}$ and the other additional matrices are as defined in Table 2.

$$\mathbf{A}_{dT} = \mathbf{D}_T\mathbf{A}_d, \mathbf{A}_{dL} = \mathbf{D}_L\mathbf{A}_d, \mathbf{B}_{1dT} = \mathbf{D}_T\mathbf{B}_{1d}, \mathbf{B}_{1dL} = \mathbf{D}_L\mathbf{B}_{1d}\mathbf{E}_{dT} = \mathbf{D}_T\mathbf{E}_d, \mathbf{E}_{dL} = \mathbf{D}_L\mathbf{E}_d. \tag{16}$$

4. GA-LSTM Control System

The FPEEA and GA-fuzzy control laws have been applied to LSCIS [36, 37]. In FPEEA, the ground motion characteristics of an earthquake are divided into six intervals according to their energy distributions before the arrival of the main strike [36] to determine the potential energy weighting factor QE_p. However, as only six weighted control parameters with high degree of discreteness can be selected in the FPEEA, the GA-fuzzy control was used to further quantify the characteristics of near-fault and far-field earthquakes on the basis of a quantitative index [37]. To adjust QE_p, two parameters, namely, NF ratio and predicted PGA, were used to establish a fuzzy surface in the GA-fuzzy control [37].

However, these two control laws have defects. First, the energy intervals in FPEEA have low sensitivity to ground motion characteristics, and the GA-fuzzy control may misclassify near-fault and far-field earthquakes. Second, if insufficient data are available, both the FPEEA and GA-fuzzy control would exhibit low performance levels. Accordingly, the GA-LSTM system, a method based on LSTM, was proposed in this study for classifying earthquakes. Moreover, the PEER ground motion database was adopted to analyze the "sensitivity" of earthquake events. That is, some earthquake motions are sensitive to variations in QE_p, and changing QE_p can improve the performance of the system; these earthquakes were denoted "sensitive" earthquakes in this study. Other earthquakes for which modifying the weights did not affect system performance were denoted "insensitive" earthquakes. The proposed procedure was intended to optimize the control efficiency.

4.1. Earthquake Sensitivity and $\mathbf{QE_p}$. According to equation (15), the weighting factor QE_p is a key control parameter. The numerical model for the LSCIS (Figures 5 and 6) was simulated using the system parameters listed in Table 3 to evaluate earthquake sensitivity. The specimen parameters listed in Table 3 were obtained by a series of the system identification procedures before the experimental

Table 2: Details of each control coefficient.

Coef.	Values
$a_1[n]$	$\mathbf{z}[n]^T\mathbf{B}_{1d}{}^T\mathbf{D}_2{}^T\mathbf{M}\mathbf{D}_2\mathbf{B}_{1d}\mathbf{z}[n]$
$b_{2,\text{iso}}[n]$	$\mathbf{B}_{1dL}\mathbf{z}[n](\mathbf{A}_{dL}\mathbf{z}[n] + \mathbf{E}_{dL}\ddot{x}_g[n])k_{r0}$
$b_{2,\text{sup}}[n]$	$\mathbf{B}_{1dL}\mathbf{z}[n]k_s(2(\mathbf{A}_{dL}\mathbf{z}[n] + \mathbf{E}_{dL}\ddot{x}_g[n]) + (\mathbf{A}_{dT}\mathbf{z}[n] + \mathbf{E}_{dT}\ddot{x}_g[n]))+ \mathbf{B}_{1dT}\mathbf{z}[n]k_s\ (2(\mathbf{A}_{dT}\mathbf{z}[n] + \mathbf{E}_{dT}\ddot{x}_g[n]) + (\mathbf{A}_{dL}\mathbf{z}[n] + \mathbf{E}_{dL}\ddot{x}_g[n]))$
$a_2[n]$	$\mathbf{z}[n]^T\mathbf{B}_{1d}{}^T\mathbf{D}_2{}^T\mathbf{M}\mathbf{D}_2(\mathbf{A}_d\mathbf{z}[n] + \mathbf{E}_d\ddot{x}_g[n]) + \mathbf{D}\mathbf{M}\mathbf{D}_2\mathbf{B}_{1d}\mathbf{z}[n]\dot{x}_g[n]$
$b_{3,\text{iso}}[n]$	$0.5(\mathbf{A}_{dL}\mathbf{z}[n])^2k_{r0} + 0.5(\mathbf{E}_{dL}\ddot{x}_g[n])k_{r0} + \mathbf{A}_{dL}\mathbf{z}[n]\mathbf{E}_{dL}\ddot{x}_g[n]k_{r0}$
$b_{3,\text{sup}}[n]$	$0.5(\mathbf{A}_{dL}\mathbf{z}[n])^2k_s + 0.5(\mathbf{E}_{dL}\ddot{x}_g[n])k_s + \mathbf{A}_{dL}\mathbf{z}[n]\mathbf{E}_{dL}\ddot{x}_g[n]k_s + 0.5(\mathbf{A}_{dT}\mathbf{z}[n])^2k_s + 0.5(\mathbf{E}_{dT}\ddot{x}_g[n])k_s + \mathbf{A}_{dT}\mathbf{z}[n]\mathbf{E}_{dT}\ddot{x}_g[n]k_s - 0.5\mathbf{A}_{dT}\mathbf{z}[n]\mathbf{E}_{dL}\ddot{x}_g[n]k_s - 0.5\mathbf{A}_{dL}\mathbf{z}\ [n]\mathbf{E}_{dT}\ddot{x}_g[n]k_s$

Table 3: Parameters of superstructure and isolation layer.

	Project	Values
Superstructure	Superstructure mass (ms)	22.01 kg
	Horizontal strength (ks)	3400 N/m
	Horizontal damping (cs)	1.971 N-sec/m
	Natural frequency (f_s)	1.98 Hz
Isolation layer	Isolation platform mass (m_b)	38.445 kg
	Leverage length (L)	0.38 m
	Spring stiffness (k_{r0})	600 N/m
	Coefficient of friction (μ)	0.008
	Leverage pivot moving range (x_p)	(0.0505 L, −0.191 L) m
	Isolation stiffness range (k_r)	($-0.8k_{r0}$, $0.5k_{r0}$) N/m

verification detailed in Section 6. For the system identification of the superstructure, a 22.01 kg mass block is added on the top of the superstructure. Acceleration and displacement signals are recorded under a free vibration test, and the natural frequency F_s of the superstructure can be identified as 1.98 Hz through Fast Fourier Transform (FFT) analysis. The hysteresis loop was then drawn together with the displacement signal to determine the stiffness value k_s of the superstructure, which is approximately 3400 N/m.

For identifying the parameters of the isolation layer, the pivot of the LSCIS mechanism is fixed at the origin, and the initial stiffness value k_{r0} and friction coefficient μ were calculated by drawing a hysteresis loop of the isolation layer obtained from another free vibration test to decide spring stiffness k_{r0}, which turn out to be 600 N/m. The optimal stiffness increment $\Delta k_{r,\text{opt}}[n]$ was calculated using equation (15). The range of the control parameter QE_p was set to 0–200, and the pivot limit parameter R was set to 8×10^{-8}. The optimal value of QE_p typically depends on the control goal; for near-fault earthquakes, the control goal is to minimize the peak displacement of the isolation layer. For far-field earthquakes, the control goal is to minimize the peak acceleration of the superstructure.

Sensitivity of an earthquake can be determined from the characteristics of the ground motion and also from the properties of the structural system that withstand the earthquakes. This study shows the control results of an elastic structure; however, the structure condition is also adjustable in each step, including LSCIS control law, GA-LSTM control system, and numerical simulation. On the basis of the simulation results derived for peak isolation displacement, near-fault earthquakes could be divided into sensitive and insensitive earthquakes in this study. Near-fault earthquake No. 1227-1 was determined to be a typical example of a sensitive earthquake (Figure 7(a)); the optimal value of QE_p that could minimize the peak isolation displacement could be derived for this earthquake. Moreover, earthquake No. 728-1 was determined to be a typical example of an insensitive earthquake (Figure 7(b)); the value of the peak isolation displacement was insensitive to variations in QE_p. For insensitive earthquakes, determining the optimal QE_p value was noted to be challenging.

The QE_p values that could minimize peak isolation displacement for each sensitive near-fault earthquake are plotted in Figure 7(c); the horizontal axis of the figure represents the earthquake number, and the vertical axis represents the corresponding optimal QE_p value. The complex distribution of sensitive near-fault earthquakes in Figure 7(c) indicates that a module for determining the optimal QE_p would be necessary for practical applications.

Sensitive far-field earthquakes were also identified by removing cases for which modifying QE_p substantially affected the peak acceleration of the superstructure. Earthquake No. 359-2 was noted to be a typical example of a sensitive far-field earthquake (Figure 8(a)); an optimal QE_p value that could minimize the peak acceleration of the superstructure could be derived for this earthquake. By contrast, earthquake No. 344-1 was determined to be a representative example of an insensitive far-field earthquake (Figure 8(b)).

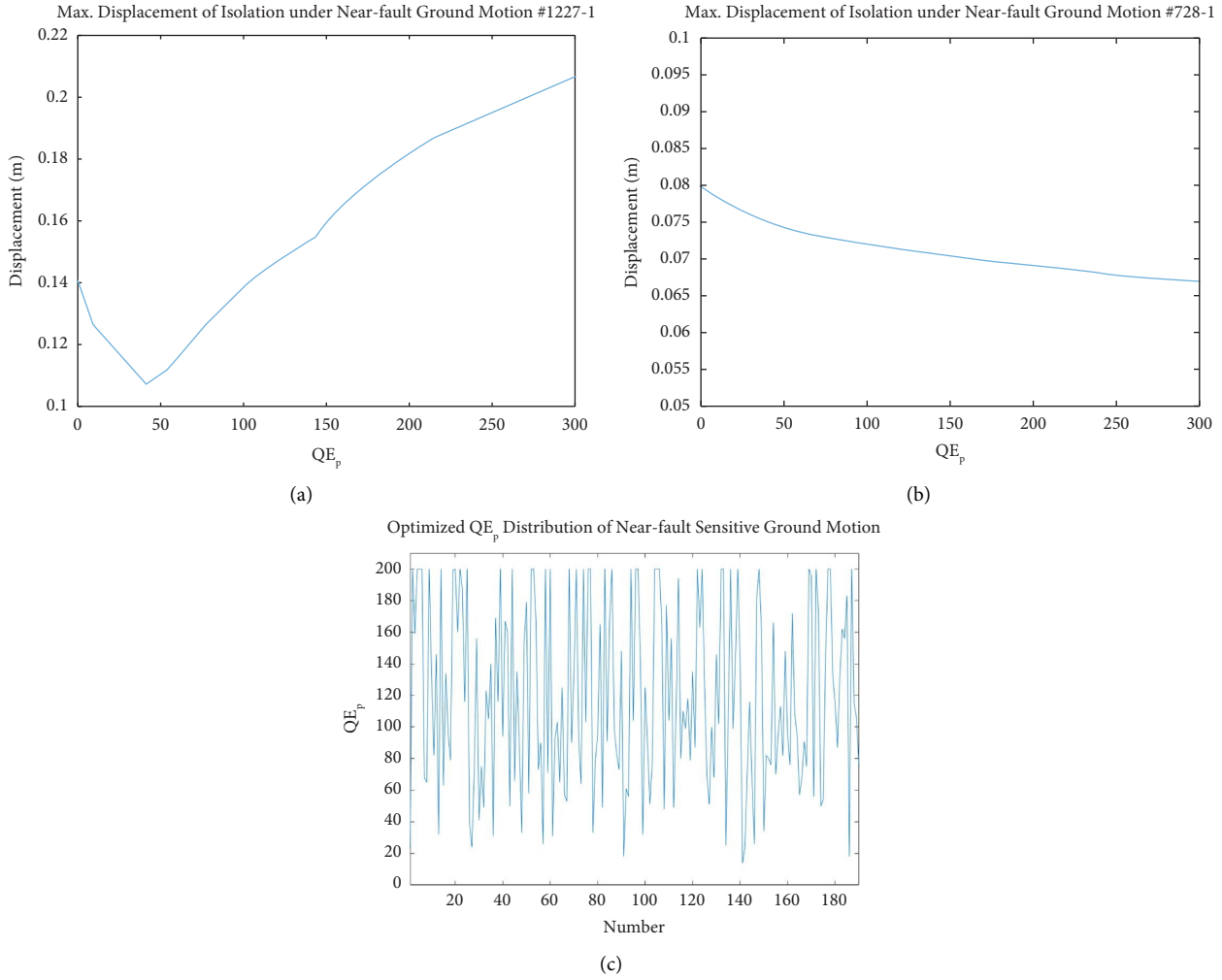

FIGURE 7: Sensitivity analysis of near-fault earthquakes for peak isolation displacement. (a) Sensitive earthquake #1227-1. (b) Nonsensitive earthquake #728-1. (c) Distribution of QE_p.

The optimized QE_p value for each of the selected sensitive far-field earthquakes and the overall distribution of these values are presented in Figure 8(c). Most QE_p values for sensitive far-field earthquakes were low; thus, the corresponding average QE_p value in Figure 8(c) was used for the control law for these earthquakes in this study.

4.2. Fuzzy Surfaces for near-Fault Earthquakes. As illustrated in Figure 7(c), the optimal value of QE_p varied for sensitive near-fault earthquakes. To determine this value, the GA-Fuzzy control based on the NF ratio and predicted PGA was applied [35]. A continuous surface was then established by fuzzifying the optimal QE_p as a function of the NF ratio and predicted PGA.

The predicted PGA was estimated through a support vector regression model during the first 3 seconds before the earthquake trigger point by using the following input parameters: absolute value of acceleration (P_a), which represents the maximum absolute acceleration, absolute value of velocity (P_v), which represents the maximum absolute velocity, absolute value of displacement (P_d), which represents the maximum absolute displacement, effective predominant period (τ_c), integral of the squared velocity (IV2), and cumulative absolute velocity (CAV) [37]. Details regarding τ_c, IV2, and CAV are presented as follows:

$$\tau_c = \frac{2\pi}{\sqrt{r}}, \text{where } r = \frac{\int_0^{t_p} \dot{u}(t)^2 \mathrm{d}t}{\int_0^{t_p} u(t)^2 \mathrm{d}t}, \tag{17}$$

$$\mathrm{IV2} = \int_0^{t_p} \dot{u}(t)^2 \mathrm{d}t, \tag{18}$$

$$\mathrm{CAV} = \int_0^{t_p} |\ddot{u}(t)| \mathrm{d}t, \tag{19}$$

where $u(t)$ is the vertical displacement, $\dot{u}(t)$ is the vertical velocity, $\ddot{u}(t)$ is the vertical acceleration, and t_p was set to 3 seconds.

In addition to the aforementioned six parameters, two additional parameters were used to calculate the NF ratio: the horizontal high-frequency accumulated acceleration

energy $(C_{Ea})_{\text{horizontal}}$ and accumulated velocity $(C_{Ev})_{\text{horizontal}}$ [35]. The NF ratio was then calculated as a function of the eight parameters, as expressed in the following equation:

$$\begin{aligned}
\text{NF Ratio} &= \sum_{i=1}^{8}\left\{\left[\frac{x_i}{(\overline{x_{iN}}+\overline{x_{iF}}/2)}\right]\times\frac{\overline{x_{iN}}}{\overline{x_{iF}}}\right\},\\
x_1 &= P_a,\\
x_2 &= P_v,\\
x_3 &= P_d,\\
x_4 &= \tau_c,\\
x_5 &= \text{IV2},\\
x_6 &= \text{CAV},\\
x_7 &= (C_{Ea})_{\text{horizontal}},\\
x_8 &= (C_{Ev})_{\text{horizontal}},
\end{aligned} \tag{20}$$

where $\overline{x_{iN}}$ and $\overline{x_{iF}}$ are the average values of x_i for near-fault and far-range earthquakes, respectively. Equation (20) was used to derive the NF ratio for each earthquake in this study. The average value of each parameter and the NF ratio are listed in Table 4.

The NF ratio and predicted PGA values for selected near-fault earthquakes are plotted in Figure 9. Based on the earthquake distribution and quantity, these earthquakes were classified into 20 blocks (Figure 10). The QE_p value for each block was estimated on the basis of the optimal value for the earthquake events in the block.

The average QE_p values derived for selected sensitive near-fault earthquakes are presented in Figure 11. Because blocks (II, VL), (III, VL), and (IV, VS) had no sensitive earthquakes (Figure 10), the control parameters for these three blocks were determined by taking the average of the parameters for the two adjacent blocks. These discrete values were further smoothed using a fuzzy controller based on the NF ratio and predicted PGA (horizontal and vertical axes of Figure 11). The membership function of the NF ratio comprised five functions (I–V), and the membership function of the predicted PGA comprised four functions VL, SL, SS, and VS where VL is very large; SL is slightly large; SS is slightly small, and VS is very small. The output membership function was used to classify the earthquakes into 18 groups according to the value of QE_p in Figure 11. Finally, fuzzy inference was performed using Mamdani fuzzy logic, and the center-of-gravity method was applied for defuzzification. The contour of the control parameter QE_p as a function of the predicted PGA and NF ratio is presented in Figure 12.

In the improved GA-LSTM control system, the LSTM prediction module is first employed to detect the ground motion characteristics. If an earthquake is detected as a near-fault earthquake, the optimal QE_p can be quickly determined by the established fuzzy system. Otherwise, QE_p is set to 23 if the earthquake is a far-field earthquake. In this research, structural conditions are considered and coupled into the analytical model in the design stage of the proposed GA-LSTM control system. Thus, the proposed GA-LSTM control system can be applied to all types of structures with satisfactory performance. Moreover, the robustness and reliability of the GA-LSTM control system can also be supported by the fuzzy logic core.

5. Numerical Simulations

The control performance of the proposed LSCIS along with the GA-LSTM system was evaluated numerically for two sensitive earthquakes and compared with the performance of other control laws. The selected earthquakes were not those used to design the controller and are outlined as follows:

(1) Christchurch earthquake (2011): station, Shirley Library; magnitude, 6.2; peak acceleration, 3.4152 m/s^2 (0.348 g); PEER Database Sequence #8130-2 (near-fault)

(2) Coalinga earthquake (1983): station, Parkfield Fault Zone 4; magnitude, 6.36; peak acceleration, 1.1876 m/s^2 (0.121 g); PEER Database Sequence #343-2 (far-field)

The predicted LSTM labels for the near-fault Christchurch earthquake and far-field Coalinga earthquake were 0.999 and 0.054, respectively, indicating that the network could correctly classify the earthquakes. The two earthquakes were then input into the numerical model for the LSCIS, and the model was executed using the system parameters listed in Table 3. The time histories of the structural responses, including superstructure acceleration, isolation layer displacement, and pivot displacement, are illustrated in Figures 13–16. In addition, the displacement (x_s, x_b), velocity $(\dot{x}_s, \dot{x}_b)$, and acceleration $(\ddot{x}_s, \ddot{x}_b)$ of the LSCIS under different control laws are listed in Tables 5 and 6; the subscripts s and b represent the superstructure and isolation layer, respectively.

5.1. Control Performance for the near-Fault Christchurch Earthquake (2011). As presented in Table 5, for the near-fault Christchurch earthquake, the isolation displacement x_b observed for the GA-LSTM system was 17.5 cm, which was substantially lower than that observed for passive control (24 cm), indicating that the GA-LSTM system has superior performance. Because of the reduction of the isolation displacement, the peak superstructure displacement, the velocity of the isolation layer, and the velocity of the superstructure decreased. However, the difference in the peak acceleration was small between the two methods.

As shown in Figure 13, the GA-LSTM system also outperformed the FPEEA it reduced the isolation displacement and superstructure acceleration 7–10 s after the mainshock. The FPEEA erroneously treated this earthquake as a far-field event, reducing its ability to control the isolation displacement. Moreover, the improper control of

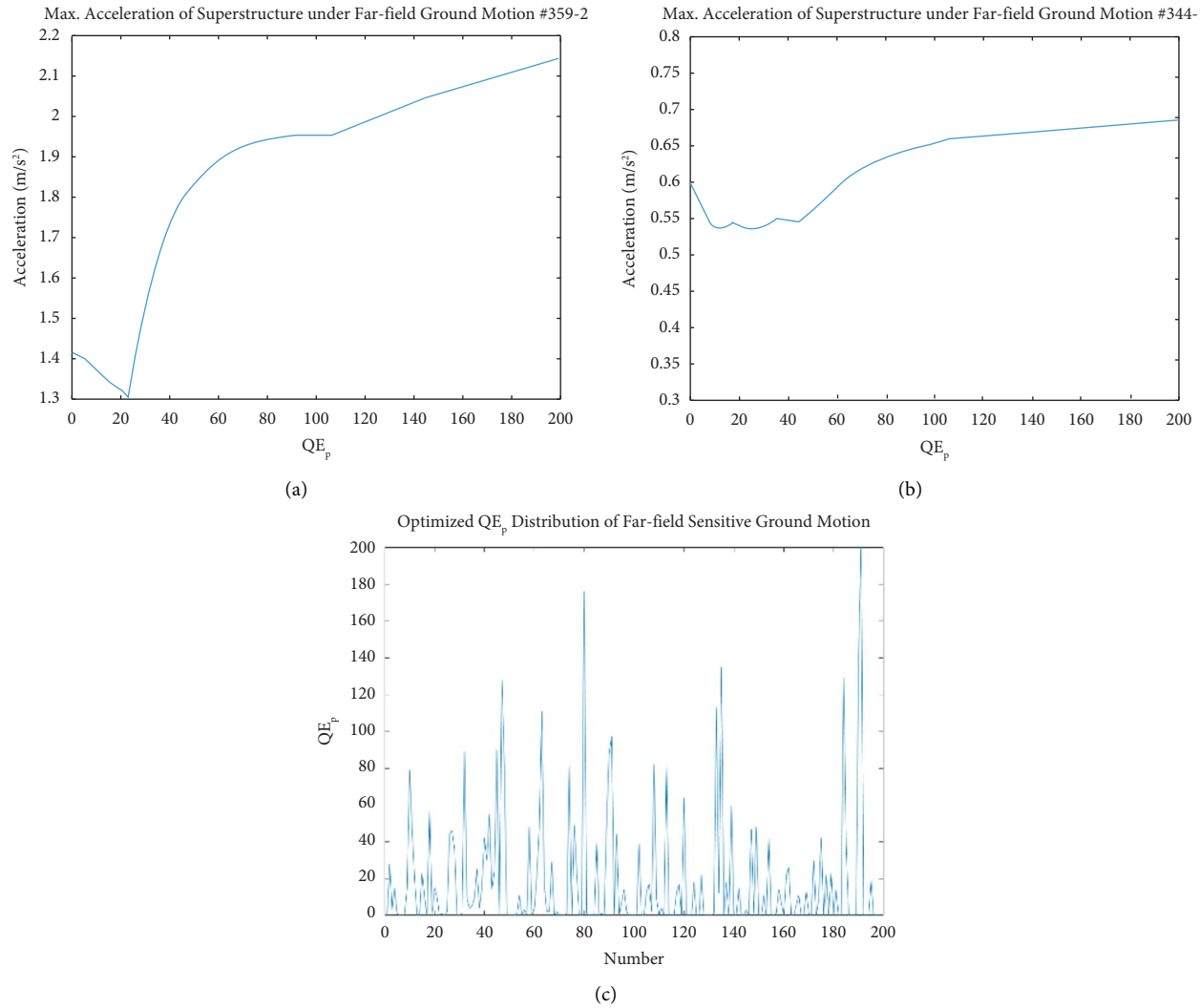

Figure 8: Sensitivity analysis of far-field earthquakes for peak structural acceleration. (a) Sensitive earthquake #359-2. (b) Nonsensitive earthquake #344-1. (c) Distribution of QE_p.

Table 4: Average values of the parameters.

	Near-fault GMs	Far-field GMs
P_a (cm/s^2)	0.1769	0.0374
P_v (cm/s)	6.7413	1.5630
P_d (cm)	2.6831	0.6138
CAV (cm/s)	0.1023	0.0247
IV2 (cm^2/s)	50.984	1.5872
τ_c (sec)	3.9576	4.0131
$(C_{Ea})_{\text{horizontal}}$ (cm^2/s^4)	0.0209	0.0039
$(C_{Ev})_{\text{horizontal}}$ (cm/s)	0.9708	0.1249
NF ratio	9.4968	3.8355

isolation displacement reduced the control of the acceleration response. Thus, the poor control results derived for the FPEEA can be attributed to the fact that the FPEEA does not accurately determine the earthquake type.

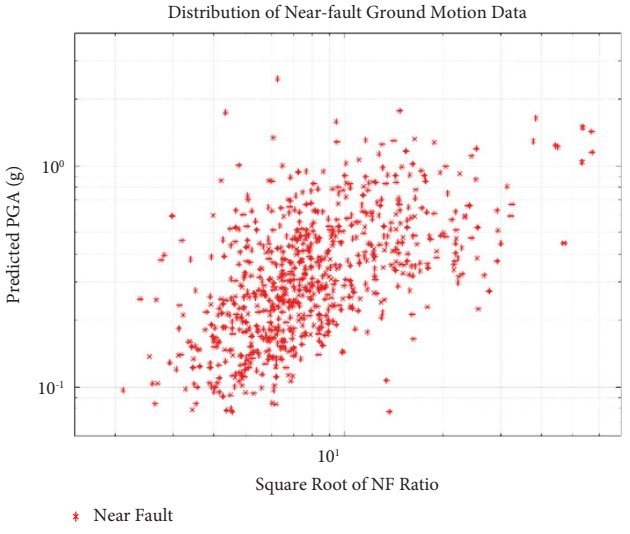

Figure 9: The NF Ratio and PGA value of near-fault earthquakes.

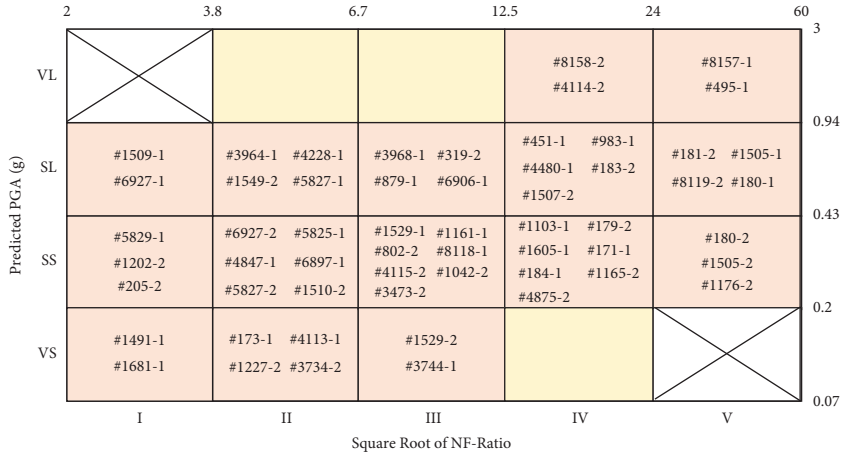

Figure 10: Selected earthquake data (sensitive near-fault earthquakes).

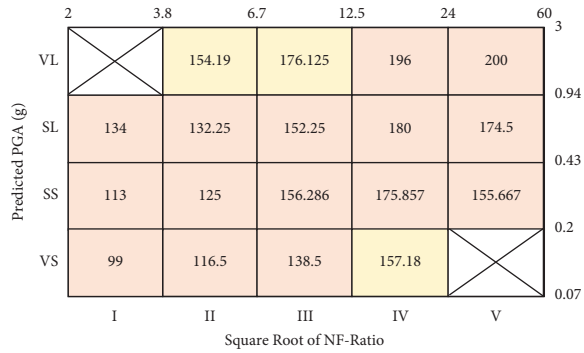

Figure 11: Results of optimized control parameters.

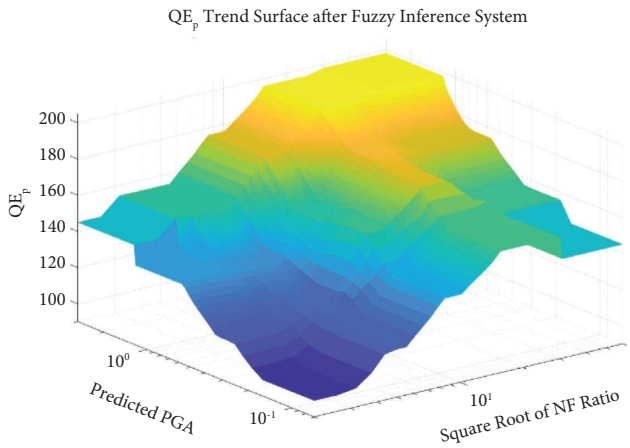

Figure 12: Fuzzy surface of QE_p.

As displayed in Figure 14, although the GA-fuzzy control and the GA-LSTM system exhibited similar responses, the isolation displacement of the GA-LSTM system was approximately 1.5 cm lower than that of the GA-fuzzy control, indicating that the GA-LSTM system had better performance. Because the GA–LSTM system can update its control laws on the basis of whether an earthquake is sensitive, the fuzzy surface established using representative earthquake events can improve its control performance.

5.2. Control Performance for the Far-Field Coalinga Earthquake (1983). As listed in Table 6, for the far-field Coalinga earthquake, the GA-LSTM system produced superior control performance for superstructure acceleration when compared with the other control laws. The peak superstructure acceleration observed for the GA-LSTM system (1.66 m/s^2) was substantially lower than that observed for the passive control (2.1 m/s^2).

As illustrated in Figure 15, although the GA-LSTM system and FPEEA exhibited similar performance levels, the GA-LSTM system had superior overall performance in the control of superstructure acceleration. Thus, control parameters determined by the GA-LSTM system can engender superior performance in reducing superstructure acceleration from the impact of far-field earthquakes.

The FPEEA was noted to exhibit superior performance to the GA-fuzzy control (Figure 16 and Table 6). Although the GA-fuzzy control parameters resulted in lower superstructure acceleration than did the FPEEA parameters (Table 6), the FPEEA engendered superior isolation acceleration, velocity, and displacement performance. Furthermore, the FPEEA achieved lower superstructure

Table 5: Peak responses of near-fault Christchurch earthquake.

Control law	$x_s\,(m)$	$x_b\,(m)$	$\dot{x}_s\,(m/s)$	$\dot{x}_b\,(m/s)$	$\ddot{x}_s\,(m/s^2)$	$\ddot{x}_b\,(m/s^2)$
Passive	0.2739 (1.000)	0.2418 (1.000)	0.9838 (1.000)	0.9394 (1.000)	4.9646 (1.000)	3.8710 (1.000)
FPEEA	0.2403 (0.877)	0.2159 (0.893)	1.0553 (1.073)	0.9555 (1.017)	7.2437 (1.459)	5.7031 (1.473)
GA-fuzzy	0.2157 (0.788)	0.1881 (0.778)	0.7911 (0.804)	0.7754 (0.825)	4.5986 (0.926)	3.8003 (0.982)
GA-LSTM	0.2006 (0.732)	0.1742 (0.720)	0.7412 (0.753)	0.7204 (0.767)	4.3079 (0.868)	3.4468 (0.890)

Note. The numbers in parentheses represent the ratio to the peak response of the passive control.

Table 6: Peak responses of the far-field Coalinga earthquake.

Control law	$x_s\,(m)$	$x_b\,(m)$	$\dot{x}_s\,(m/s)$	$\dot{x}_b\,(m/s)$	$\ddot{x}_s\,(m/s^2)$	$\ddot{x}_b\,(m/s^2)$
Passive	0.1214 (1.000)	0.1085 (1.000)	0.5159 (1.000)	0.4842 (1.000)	2.0924 (1.000)	1.8605 (1.000)
FPEEA	0.0606 (0.500)	0.0529 (0.488)	0.3274 (0.635)	0.3027 (0.625)	1.9564 (0.935)	1.3123 (0.705)
GA-fuzzy	0.0762 (0.628)	0.0668 (0.616)	0.3633 (0.704)	0.3463 (0.715)	1.7104 (0.817)	1.4138 (0.760)
GA-LSTM	0.0632 (0.521)	0.0557 (0.514)	0.3278 (0.635)	0.3044 (0.629)	1.6644 (0.795)	1.1143 (0.599)

Note. The numbers in parentheses represent the ratio to the peak responses of the passive control.

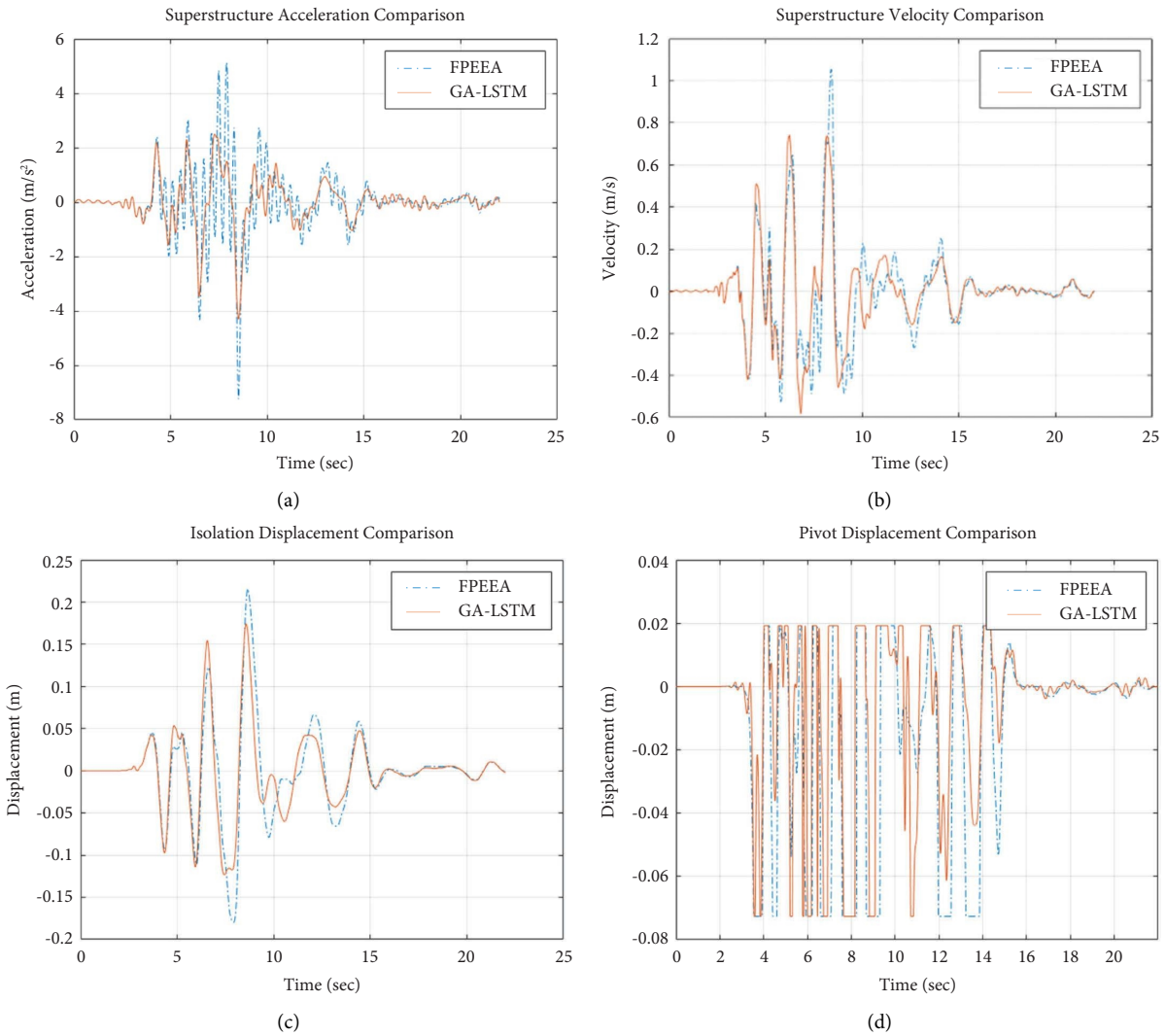

Figure 13: Comparison between the responses of FPEEA and GA-LSTM (near-fault Christchurch earthquake). (a) Superstructure acceleration. (b) Superstructure velocity. (c) Isolation layer displacement. (d) Pivot displacement.

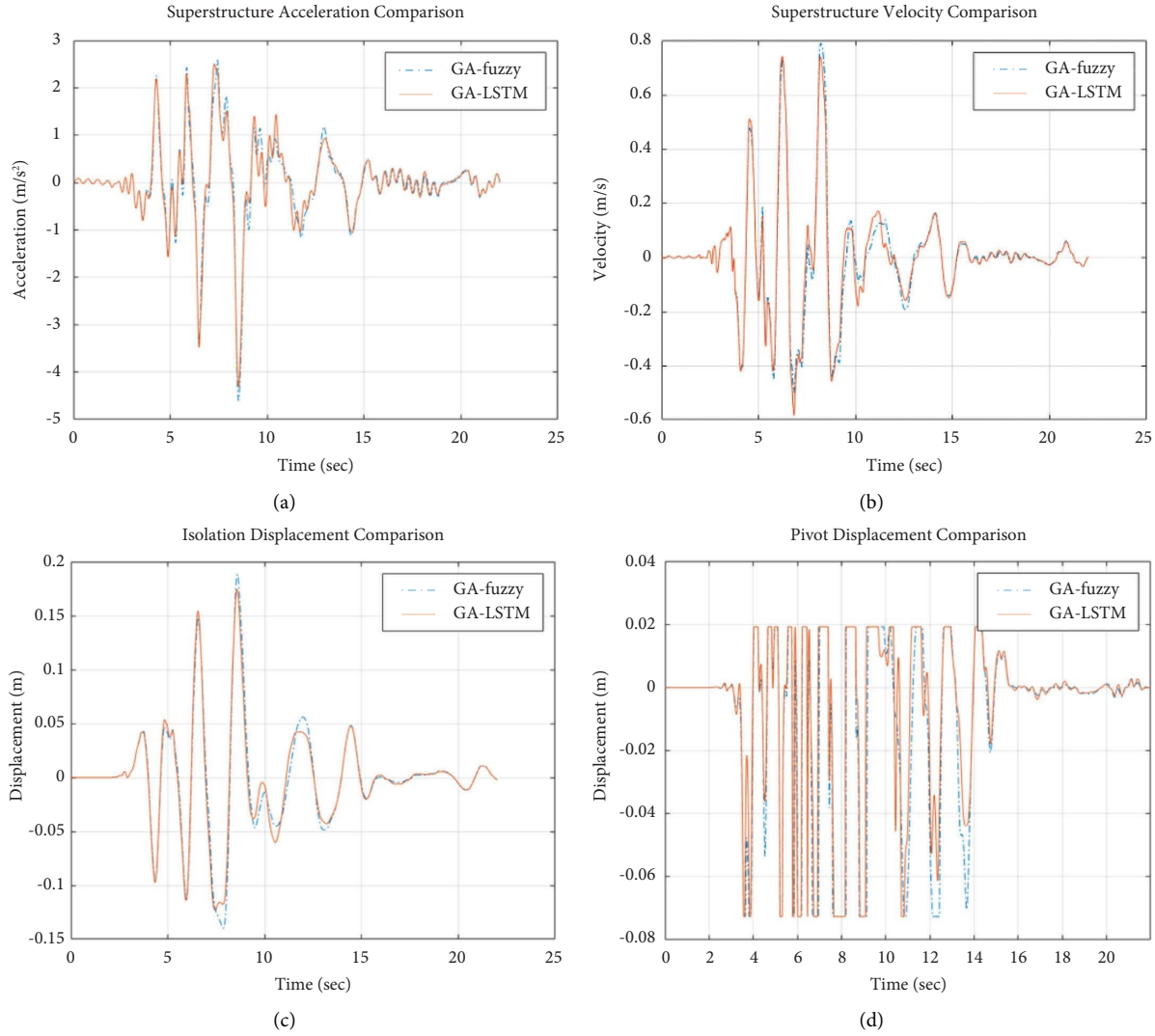

FIGURE 14: Comparison between the responses of GA-fuzzy and GA-LSTM (near-fault Christchurch earthquake). (a) Superstructure acceleration. (b) Superstructure velocity. (c) Isolation layer displacement, (d) Pivot displacement.

displacement and velocity than did the GA-fuzzy control. Thus, both the GA-LSTM system and FPEEA can select better control parameters than the GA-fuzzy control (Figures 15 and 16). Moreover, the control parameters identified by the GA-LSTM system through the sensitivity analysis for far-field earthquakes were better-tailored compared with those identified using previous control laws.

6. Shaking Table Experiment

To experimentally verify the feasibility of the proposed GA-LSTM system, a shaking table test following the system identification procedure in Section 4.1 was conducted in accordance with the flowchart in Figure 17, and the properties of the shaking table and specimen are listed in Table 7. The test setup of the LSCIS experiment is displayed in Figure 18. The LSCIS comprises the superstructure and the isolation layer, which were both equipped with sensors in the experiment (Figure 19). The input ground velocity and acceleration from the database and the measured responses of the specimen were recorded at a sampling frequency of 100 Hz through USB-6218 and recorded by the LabVIEW controller. On the basis of these signals, the GA-LSTM control law was implemented, and the optimal stiffness increment $\Delta k_{r,\mathrm{opt}}[n]$ and pivot position $x_p[n]$ for the LSCIS were determined in real time.

As the shaking table used in this research has a limited stroke of 25 cm, the near-fault earthquake adopted in the numerical simulation cannot be executed. Therefore, in the shaking table experiment, two earthquakes with relatively small stroke were chosen to make sure the experiment is conducted in safe condition. The control results for the GA-LSTM system were compared with the results for other control laws. The two selected ground motions include a near-fault earthquake and a far-field earthquake as follows.

(1) Chi-Chi Earthquake (1999): Station, TCU078; magnitude, 7.62; peak acceleration, 3.0103 m/s^2

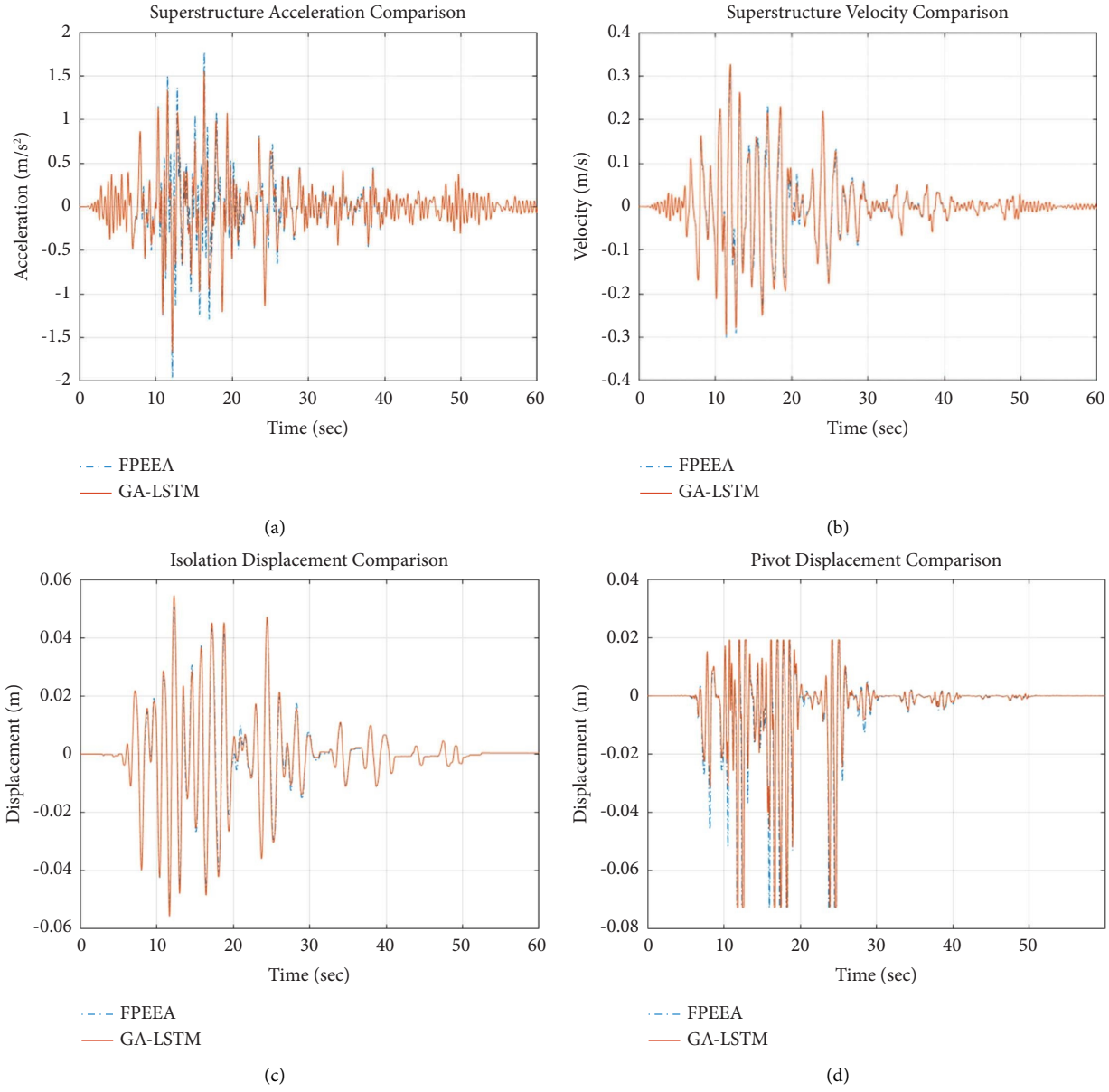

Figure 15: Comparison between the responses of FPEEA and GA-LSTM (far-field Coalinga earthquake). (a) Superstructure acceleration. (b) Superstructure velocity. (c) Isolation layer displacement. (d) Pivot displacement.

(0.307 g); PEER Database Sequence #1512-2 (near-fault)

(2) Cape Mendocino Earthquake (1992): Station, South Bay Union School; magnitude, 7.01; peak acceleration, 1.9570 m/s^2 (0.200 g); PEER Database Sequence #3751-2 (far-field)

6.1. Comparison between Experimental and Numerical Results. In order to make sure that the earthquakes used in the numerical simulation can be regenerated in the shaking table experiment, the results of the shaking table experiment and the numerical simulation obtained for the LSCIS with the GA-LSTM system under the near-fault Chi-Chi

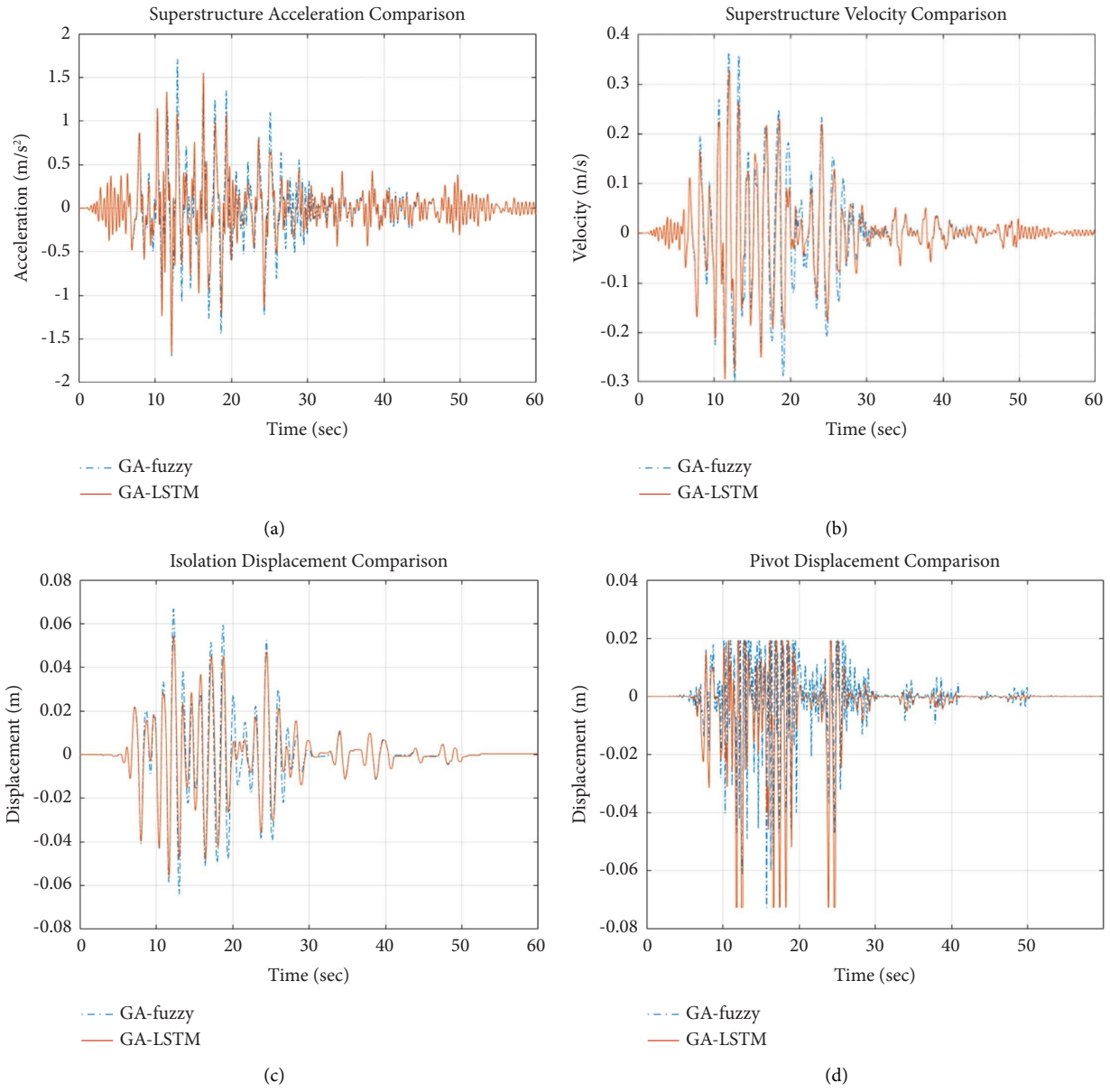

Figure 16: Comparison between the responses of GA-fuzzy and GA-LSTM (far-field Coalinga earthquake). (a) Superstructure acceleration. (b) Superstructure velocity. (c) Isolation layer displacement. (d) Pivot displacement.

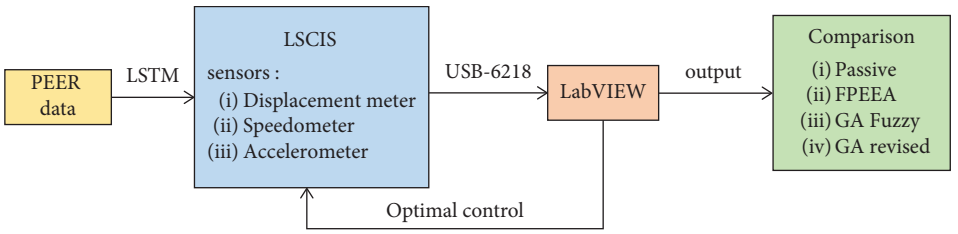

Figure 17: Experiment flowchart of shaking table test.

Table 7: Shaking table and specimen properties.

Shaking table	
Size (mm)	2500 × 1200
Steel countertop weight (kg)	800
Maximum load (kg)	1000
Maximum bending moment (kg·m)	1000
Maximum stroke (mm)	250
Maximum acceleration (gal)	800
Experimental specimen	
Size (mm)	400 × 400 × 476
Specimen weight (kg)	22.01
Natural frequency (Hz)	1.98
Damping ratio (%)	1.5

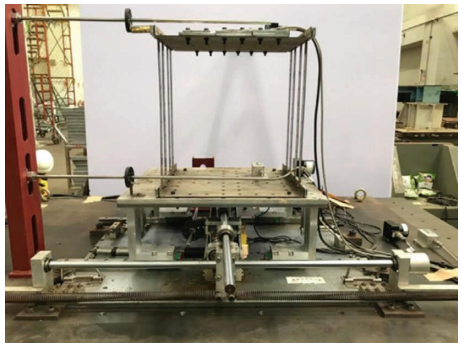

Figure 18: Test setup for the LSCIS.

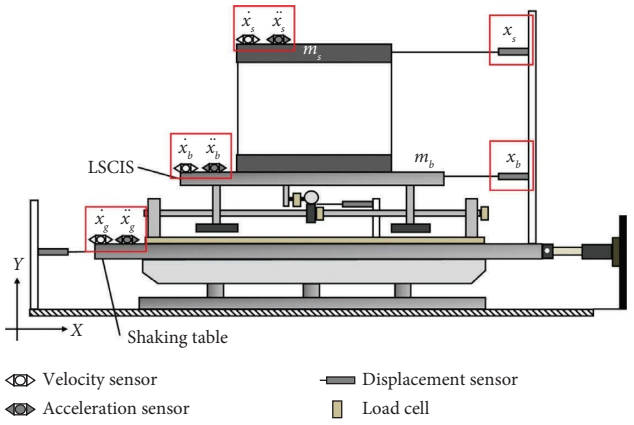

Figure 19: The instrumentation of the test.

earthquake (TCU078) were compared to prove that the performance of the proposed control law can be reliably verified. As shown in Figure 20, both the superstructure acceleration and isolation displacement had similar peak values and waveforms in the experiment and numerical simulation, further confirming the validity of the analysis model and the proposed control law.

These two earthquakes are thus be chosen for shaking table experiment in this study, and for each earthquake, the ground motion characteristics of the first 3 s seismic acceleration were first identified using the LSTM module, which classified it as a near-fault earthquake (label 0.9999). The far-field Cape Mendocino earthquake was also correctly classified (label 0.0729). The two earthquakes were reproduced using the shaking table test, and various control laws were applied to the LSCIS. The tested control laws were passive control, FPEEA, GA-fuzzy control, and GA-LSTM control.

6.2. Comparison of Control Performance for Various Control Laws

6.2.1. Control Performance for the near-Fault Chi-Chi Earthquake (1999). As presented in Table 8, for the near-

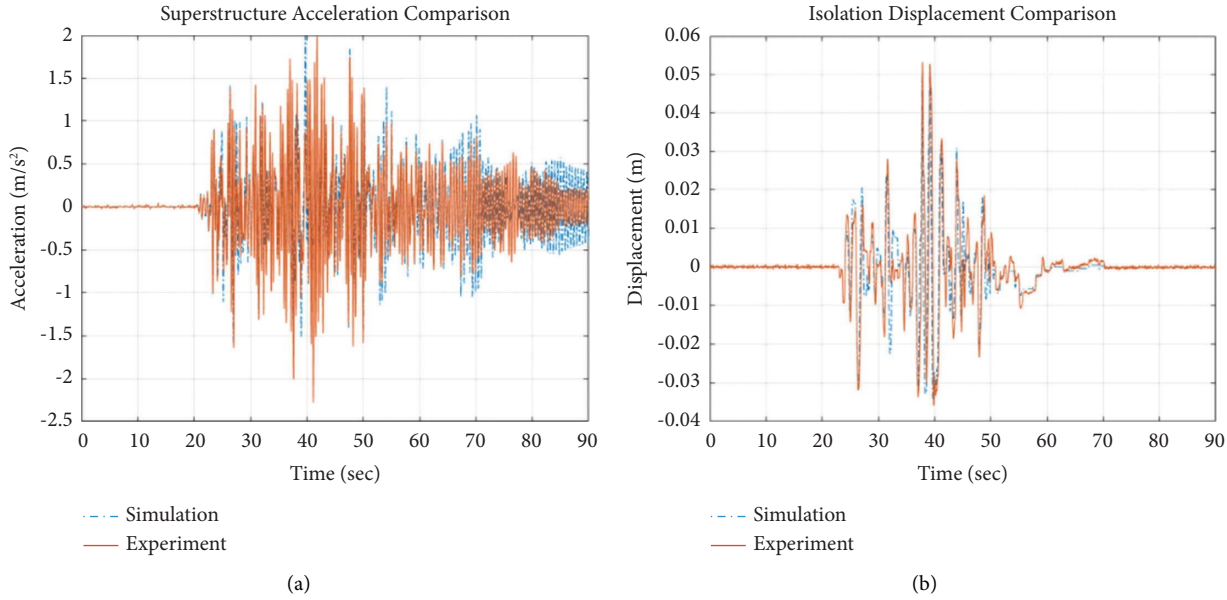

Figure 20: Comparison of experiment and numerical simulation (near-fault Chi-Chi earthquake). (a) Superstructure acceleration. (b) Isolation layer displacement.

Table 8: Peak values under near-fault Chi-Chi earthquake.

Control law	$x_s\,(m)$	$x_b\,(m)$	$\dot{x}_s\,(m/s)$	$\dot{x}_b\,(m/s)$	$\ddot{x}_s\,(m/s^2)$	$\ddot{x}_b\,(m/s^2)$
Passive	0.0822 (1.000)	0.0660 (1.000)	0.3337 (1.000)	0.2796 (1.000)	2.6680 (1.000)	2.2513 (1.000)
FPEEA	0.0614 (0.747)	0.0595 (0.902)	0.2934 (0.879)	0.2052 (0.734)	1.8872 (0.707)	1.4716 (0.654)
GA-fuzzy	0.0567 (0.690)	0.0537 (0.815)	0.3192 (0.957)	0.2270 (0.812)	2.2623 (0.848)	1.3815 (0.614)
GA-LSTM	0.0563 (0.684)	0.0533 (0.809)	0.3168 (0.950)	0.2267 (0.811)	2.2806 (0.855)	1.4398 (0.640)

Note. The numbers in parentheses represent the ratio to passive control.

fault Chi-Chi earthquake, the peak displacement of the isolation layer observed for both the GA-LSTM system and GA-fuzzy (both 5.3 cm) was excellent compared with that observed for the passive control (6.6 cm). The velocity and acceleration were also reduced because of the reduction of the isolation displacement; these results were consistent with the numerical simulation results.

As presented in Figure 21, the GA-LSTM system outperformed the FPEEA in controlling near-fault earthquakes. Therefore, the proposed ground motion characteristic prediction module can rapidly determine the optimal control parameter for a near-fault earthquake and can efficiently control the isolation displacement. The pivot displacements for the GA-LSTM system and the FPEEA are depicted and compared in Figure 21(c); the GA-LSTM system mainly relies on the positive stiffness increment region to suppress the pivot displacement response.

A comparison of the responses of the GA-fuzzy control with those of the GA-LSTM system is presented in Figure 22. The responses were noted to be similar because the QE_p values of GA-fuzzy control and the GA-LSTM system were almost identical (149 and 139); this observation was attributed to both control laws correctly identifying the ground motion as a near-fault earthquake.

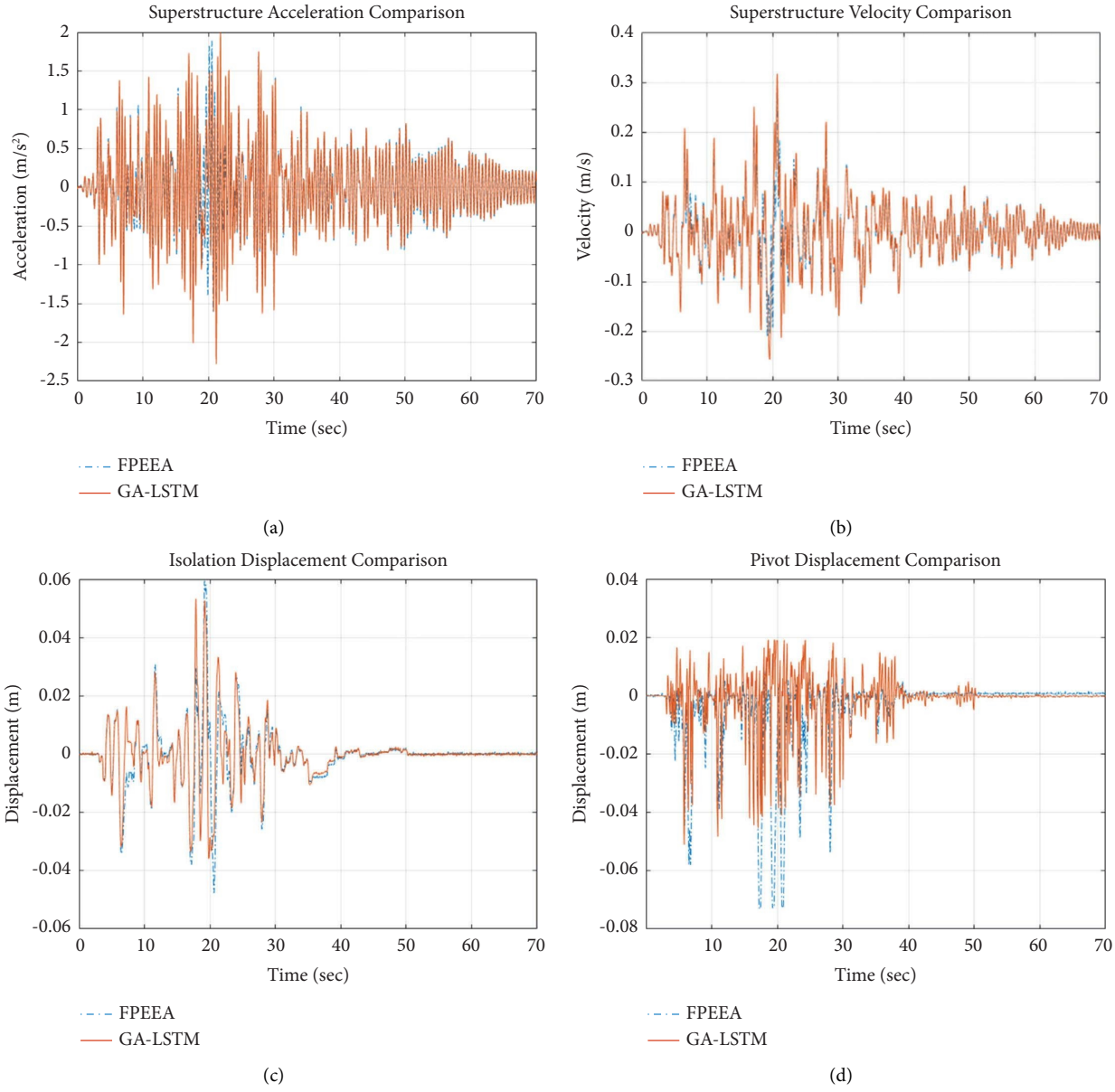

Figure 21: Comparison between FPEEA and GA-LSTM (near-fault Chi-Chi earthquake). (a) Superstructure acceleration. (b) Superstructure velocity. (c) Isolation layer displacement. (d) Pivot displacement.

6.2.2. Control Performance under Far-Field Cape Mendocino Earthquake (1992). As listed in Table 9, for the far-field earthquake Cape Mendocino, the peak superstructure acceleration observed for the GA-LSTM system was 1.43 m/s^2, substantially lower than that observed for the passive control technique (1.97 m/s^2); thus, the GA-LSTM system exhibited superior performance.

A performance comparison between the GA-LSTM system and the FPEEA (Figure 23) revealed a nonsignificant difference in responses. Nevertheless, the GA-LSTM system still exhibited superior performance, and the control parameters selected by the GA-LSTM system were effective in reducing superstructure acceleration.

As illustrated in Figure 24, the GA-LSTM system outperformed the GA-fuzzy control under the far-field earthquake, consistent with the numerical simulation results. For the GA-fuzzy control, an amplification phenomenon was noted at 7–10 s after the main shock (Figure 24(a)). Moreover, the pivot displacements observed for the GA-LSTM system (Figure 24(c)) were significantly lower than those observed for the GA-fuzzy control, indicating

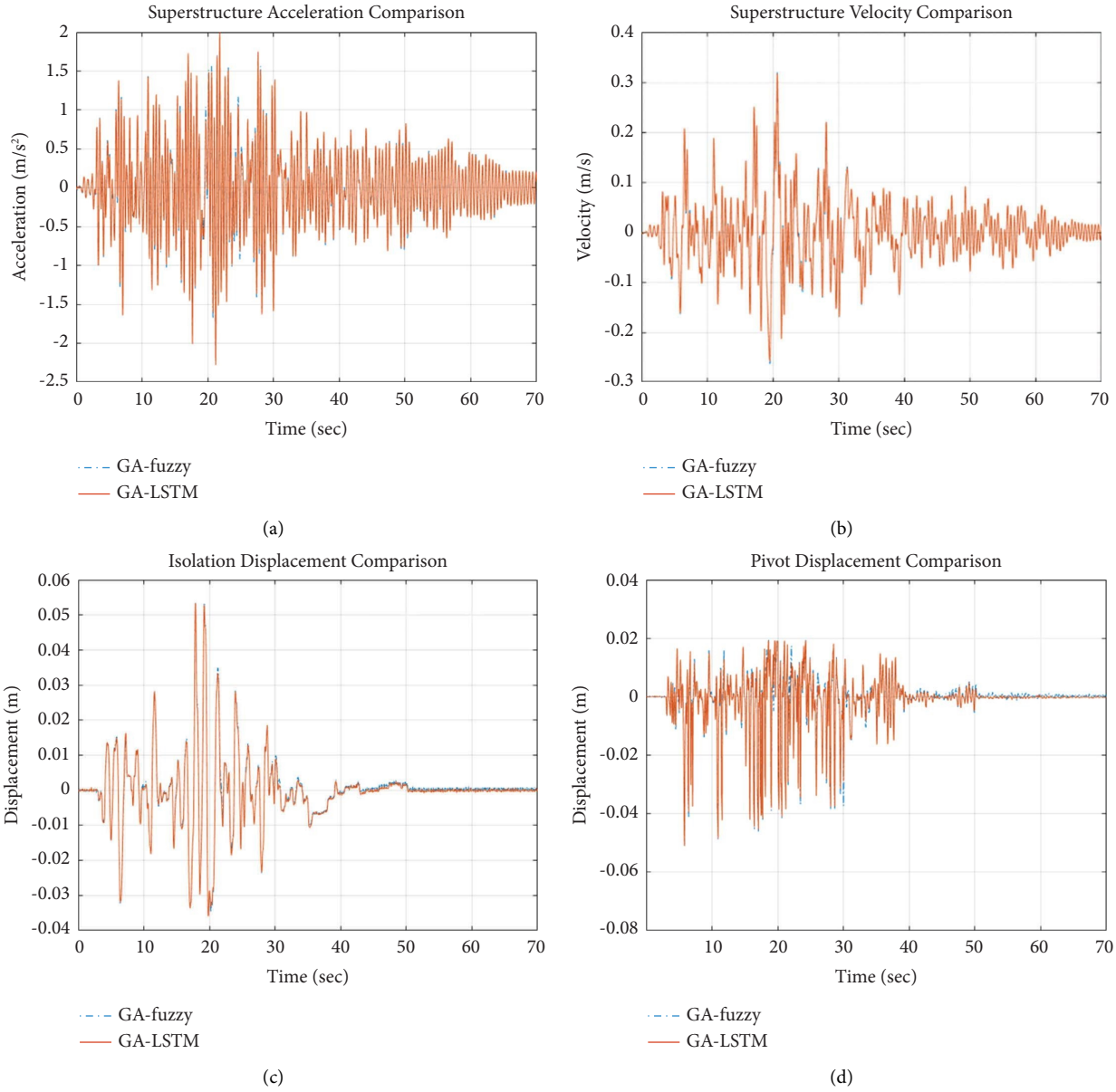

Figure 22: Comparison between GA-fuzzy and GA-LSTM (near-fault Chi-Chi earthquake). (a) Superstructure acceleration. (b) Superstructure velocity. (c) Isolation layer displacement. (d) Pivot displacement.

Table 9: Peak values of the far-field earthquake Cape Mendocino.

Control law	$x_s\,(m)$	$x_b\,(m)$	$\dot{x}_s\,(m/s)$	$\dot{x}_b\,(m/s)$	$\ddot{x}_s\,(m/s^2)$	$\ddot{x}_b\,(m/s^2)$
Passive	0.0619 (1.000)	0.0523 (1.000)	0.3022 (1.000)	0.2436 (1.000)	1.9766 (1.000)	1.2342 (1.000)
FPEEA	0.0423 (0.683)	0.0376 (0.719)	0.2522 (0.835)	0.1895 (0.778)	1.4857 (0.752)	1.0343 (0.838)
GA-fuzzy	0.0497 (0.803)	0.0407 (0.778)	0.2706 (0.895)	0.2123 (0.872)	1.7617 (0.891)	1.2448 (1.009)
GA-LSTM	0.0414 (0.668)	0.0396 (0.756)	0.2469 (0.817)	0.1883 (0.773)	1.4315 (0.724)	1.0547 (0.855)

Note. The numbers in parentheses represent the ratio to passive control.

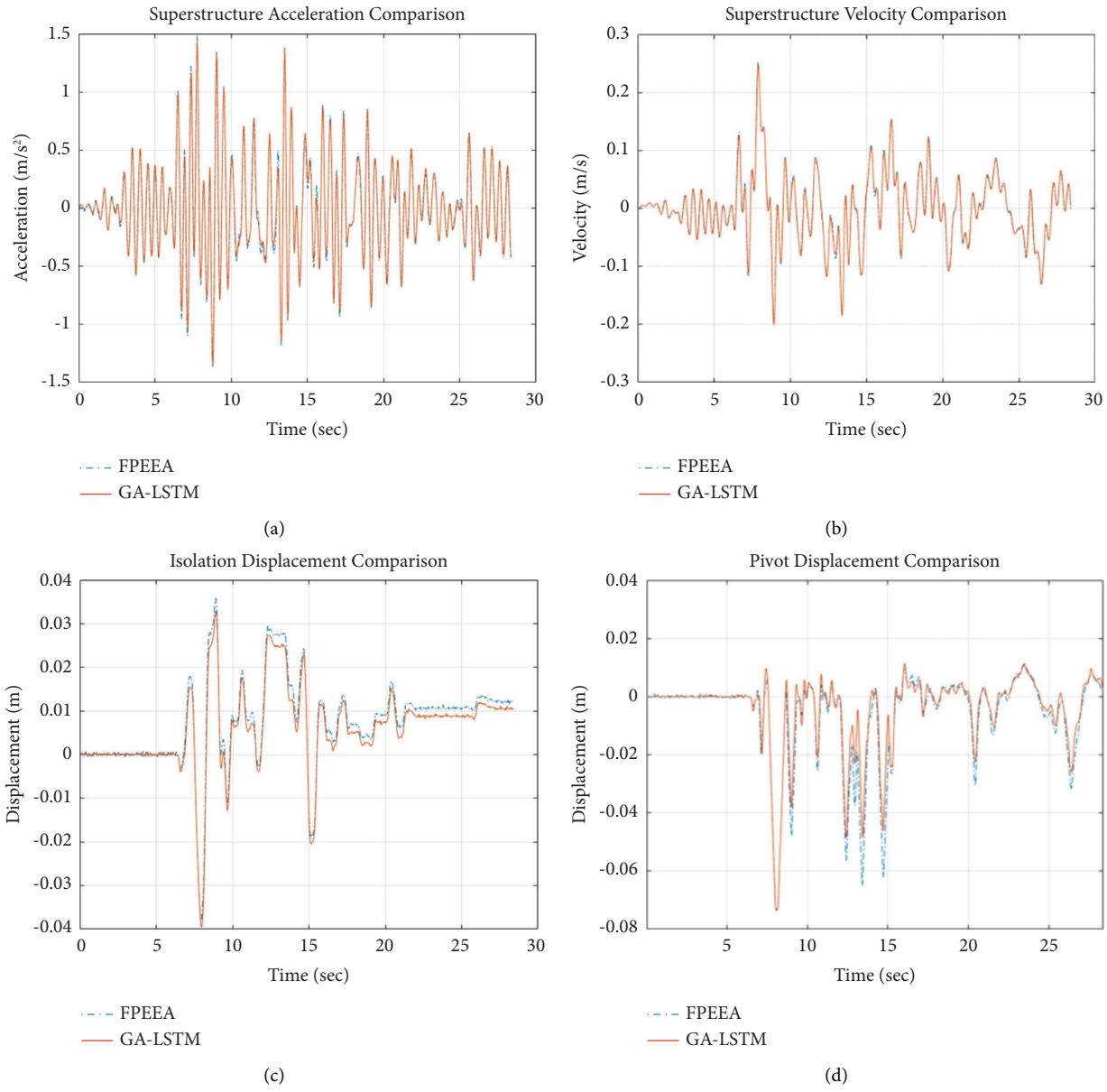

Figure 23: Comparison between FPEEA and GA-LSTM (far-field earthquake Cape Mendocino). (a) Superstructure acceleration. (b) Superstructure velocity. (c) Isolation layer displacement. (d) Pivot displacement.

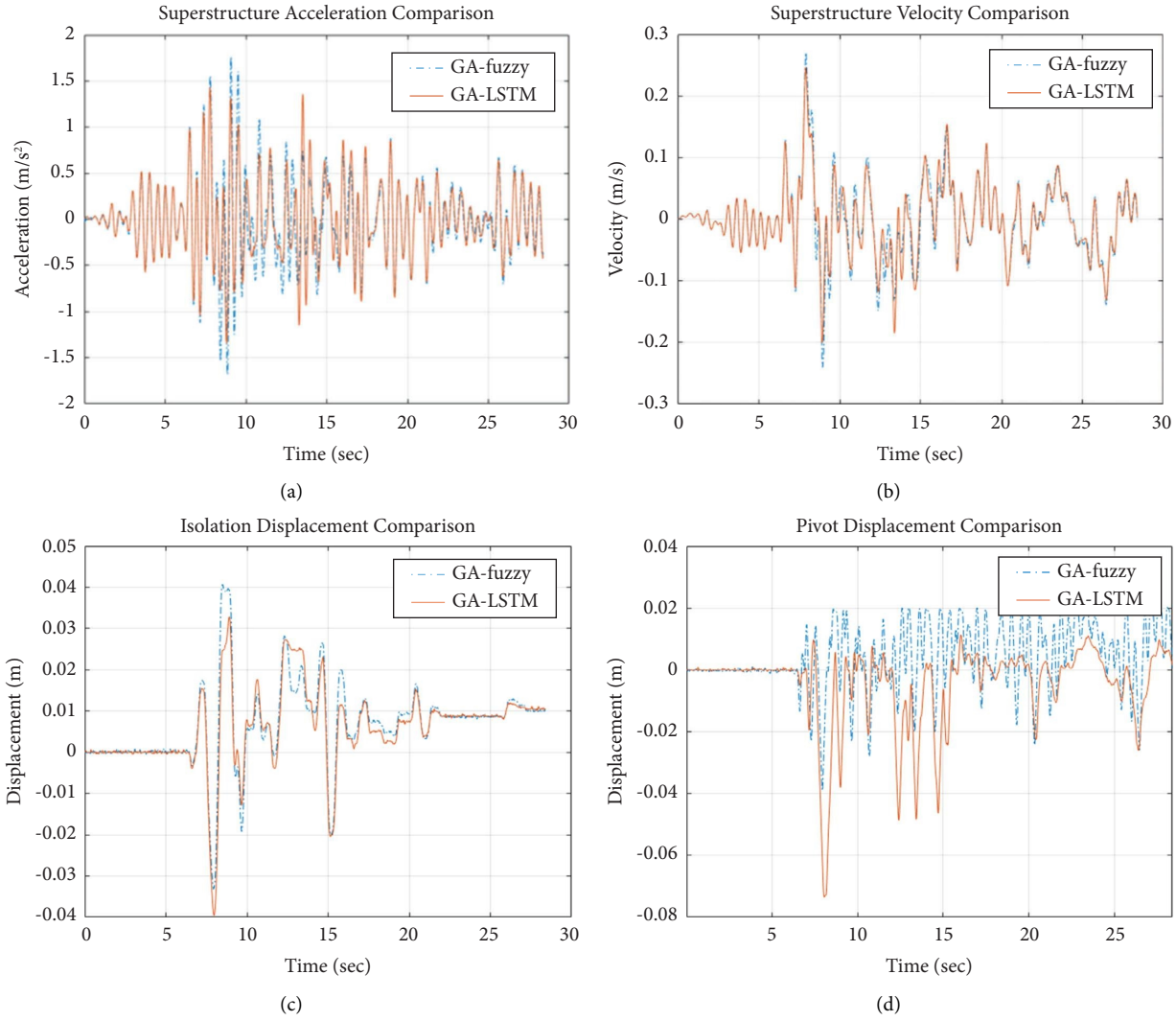

Figure 24: Comparison between GA-fuzzy and GA-LSTM (far-field earthquake Cape Mendocino). (a) Superstructure acceleration. (b) Superstructure velocity. (c) Isolation layer displacement. (d) Pivot displacement.

that the GA-LSTM system is more suitable for controlling the LSCIS during far-field earthquakes.

7. Summary and Conclusion

Ground motion characteristics substantially affect optimal semiactive control techniques. As near-fault and far-field earthquakes were slightly mixed in the controlling process of the previously developed GA-fuzzy controller, the optimal control parameters for various ground motion characteristics may still be misjudged by the fuzzy surface. Moreover, because of the insufficiency of earthquake data, the GA-fuzzy controller is sensitive to outlier cases. To overcome these shortcomings, a new controller based on LSTM (denoted the GA–LSTM system) was proposed in this study. The LSTM prediction model was first trained using data for over 1000 earthquakes and could classify near-fault and far-field earthquakes with high accuracy. An analysis of earthquake sensitivity for the optimal control parameters of the proposed GA-LSTM system further enabled a continuous function to determine the appropriate potential energy weighting for near-fault earthquakes whereas a constant value was adopted for far-field earthquakes. Numerical simulations and shaking table tests were performed to verify the performance of the GA-LSTM system. The results reveal that the GA-LSTM system successfully alleviated both superstructure acceleration and isolation layer displacement. Moreover, the pivot displacement did not have large high-frequency oscillations in the experiments, implying that the GA-LSTM system had high control stability. Both isolation layer displacement due to near-fault earthquakes and superstructure acceleration due to far-field earthquakes could be suppressed efficiently. Last, this study proposed a LSTM-based intelligent isolation system mainly follows the performance-based control strategy. It is more likely to be applied on precious vibration-sensitive devices such as cabinets in high-tech factories or precision instruments in hospital. Moreover, as these vibration-sensitive devices occupy huge economic contribution, the cost of the proposed isolation system may not be the major concern, and

the control efficiency and the functionality are focused more in this study. From the results, the proposed intelligent control system has superior performance to other control methods for all ground motion characteristics and could thus be used in practical applications.

Data Availability

Data are available upon request.

Conflicts of Interest

The authors declare that they have no conflicts of interest.

Acknowledgments

This research was supported in part by the Ministry of Science and Technology of R.O.C. (Taiwan) through grant MOST109-2625-M-009-004. This support is gratefully acknowledged.

References

[1] Y. Nakamura, "On the urgent earthquake detection and alarm system (UrEDAS)," in *Proceedings of the 9th World Conference on Earthquake Engineering*, pp. 673–678, Tokyo, Japan, August 1988.

[2] W. H. Bakun, F. G. Fischer, E. G. Jensen, and J. VanSchaack, "Early warning system for aftershocks," *International Journal of Rock Mechanics and Mining Sciences & Geomechanics Abstracts*, vol. 31, no. 6, pp. 271–365, 1994.

[3] J. M. E. Aranda, A. Jimenez, G. Ibarrola et al., "Mexico City seismic alert system," *Seismological Research Letters*, vol. 66, no. 6, pp. 42–53, 1995.

[4] P. Clemente and A. Martelli, "Seismically isolated buildings in Italy: state-of-the-art review and applications," *Soil Dynamics and Earthquake Engineering*, vol. 119, pp. 471–487, 2019.

[5] M. G. Castellano, M. Indirli, A. Martelli et al., "Seismic protection of cultural heritage using shape memory alloy devices-an EC funded project (ISTECH)," in *Proceedings of the International Post-SMiRT Conference Seminar on Seismic Isolation, Passive Energy Dissipation and Avtive Control of Vibrations of Structures*, pp. 417–443, Cheju, Korea, August 1999.

[6] G. Bongiovanni, P. Clemente, and G. Buffarini, "Analysis of the seismic response of a damaged masonry bell tower," in *Proceedings of the 12th World Conference on Earthquake Engineering*, Auckland, The New Zealand, 2000.

[7] M. Indirli, M. G. Castellano, P. Clemente, and A. Martelli, "Application of shape memory alloy devices: the rehabitation of the S. Giorgio Church bell tower," *Smart Structures and Materials: Smart Systems for Bridges, Structures, and Highways*, vol. 4330, pp. 262–272, 2001.

[8] O. E. Ozbulut and S. Hurlebaus, "Evaluation of the performance of a sliding-type base isolation system with a NiTi shape memory alloy device considering temperature effects," *Engineering Structures*, vol. 32, no. 1, pp. 238–249, 2010.

[9] K. W. Min, J. Y. Seong, and J. Kim, "Simple design procedure of a friction damper for reducing seismic responses of a single-story structure," *Engineering Structures*, vol. 32, no. 11, pp. 3539–3547, 2010.

[10] M. Mirtaheri, A. P. Zandi, S. S. Samadi, and H. R. Samani, "Numerical and experimental study of hysteretic behavior of cylindrical friction dampers," *Engineering Structures*, vol. 33, no. 12, pp. 3647–3656, 2011.

[11] O. E. Ozbulut and S. Hurlebaus, "Re-centering variable friction device for vibration control of structures subjected to near-field earthquakes," *Mechanical Systems and Signal Processing*, vol. 25, no. 8, pp. 2849–2862, 2011.

[12] L. F. F. Miguel, L. F. F. Miguel, and R. H. Lopez, "Robust design optimization of friction dampers for structural response control," *Structural Control and Health Monitoring*, vol. 21, no. 9, pp. 1240–1251, 2014.

[13] P. Clemente, G. Bongiovanni, G. Buffarini, F. Saitta, M. G. Castellano, and F. Scafati, "Effectiveness of HDRB isolation systems under low energy earthquakes," *Soil Dynamics and Earthquake Engineering*, vol. 118, pp. 207–220, 2019.

[14] A. Martelli, P. Clemente, A. De Stefano, M. Forni, and A. Salvatori, "Recent development and application of seismic isolation and energy dissipation and conditions for their correct use," *Perspectives on European Earthquake Engineering and Seismology*, vol. 1, pp. 449–488, 2014.

[15] J. C. Wu, "Modeling of an actively braced full-scale building considering control-structure interaction," *Earthquake Engineering & Structural Dynamics*, vol. 29, no. 9, pp. 1325–1342, 2000.

[16] V. Tritchkov, G. Michaelov, and S. Sarkani, "Vibration control of structures using adjustable slippage elements," *Engineering Structures*, vol. 22, no. 12, pp. 1620–1631, 2000.

[17] S. Narasimhan and S. Nagarajaiah, "ASTFT semi-active controller for base isolated buildings with variable stiffness isolation systems," *Engineering Structures*, vol. 27, no. 4, pp. 514–523, 2005.

[18] L. Y. Lu, S. Y. Chu, S. W. Yeh, and L. L. Chung, "Seismic test of least-input-energy control with ground velocity feedback for variable-stiffness isolation systems," *Journal of Sound and Vibration*, vol. 331, no. 4, pp. 767–784, 2012.

[19] D. E. Rumelhart, G. E. Hinton, and R. J. Williams, "Learning representations by back-propagating errors," *Nature*, vol. 323, no. 6088, pp. 533–536, 1986.

[20] A. Kannan, Y. Wu, P. Nguyen, T. N. Sainath, Z. Chen, and R. Prabhavalker, "An analysis of incorporating an external language model into a sequence-to-sequence model," in *Proceedings of the 2018 IEEE International Conference on Acoustics, Speech and Signal Processing (ICASSP)*, pp. 1–5828, Calgary, AB, Canada, September 2018.

[21] S. Hochreiter and J. Schmidhuber, "Long short-term memory," *Neural Computation*, vol. 9, no. 8, pp. 1735–1780, 1997.

[22] J. F. Kolen and S. C. Kremer, "Gradient flow in recurrent nets: the difficulty of learning long-term dependence," in *A Field Guide to Dynamic Recurrent Networks*, pp. 237–243, Wiley IEEE, Hoboken, NJ, USA, 2001.

[23] V. Carbune, P. Gonnet, T. Deselaers et al., "Fast multi-language LSTM-based online handwriting recognition," *International Journal on Document Analysis and Recognition*, vol. 23, no. 2, pp. 89–102, 2020.

[24] K. Pawar, R. S. Jalem, and V. Tiwari, "Stock market price prediction using LSTM RNN," *Emerging Trends in Expert Applications and Security*, pp. 493–503, Springer, Singapore, 1990.

[25] H. Apaydin, H. Feizi, M. T. Sattari, M. S. Colak, S. Shamshirband, and K. W. Chau, "Comparative analysis of recurrent neural network architectures for reservoir inflow forecasting," *Water*, vol. 12, no. 5, p. 1500, 2020.

[26] N. M. Newmark, J. A. Blume, and K. K. Kapur, "Seismic design spectra for nuclear power plants," *Journal of the Power Division*, vol. 99, no. 2, pp. 287–303, 1973.
[27] J. W. Baker, "Quantitative classification of near-fault ground motions using wavelet analysis," *Bulletin of the Seismological Society of America*, vol. 97, no. 5, pp. 1486–1501, 2007.
[28] P. Spudich, B. Rowshandel, S. K. Shahi, J. W. Baker, and B. S. J. Chiou, "Comparison of NGA-West2 directivity models," *Earthquake Spectra*, vol. 30, no. 3, pp. 1199–1221, 2014.
[29] S. K. Shahi and J. W. Baker, "An empirically calibrated framework for including the effects of near-fault directivity in probabilistic seismic hazard analysis," *Bulletin of the Seismological Society of America*, vol. 101, no. 2, pp. 742–755, 2011.
[30] G. P. Mavroeidis and A. S. Papageorgiou, "A mathematical representation of near- fault ground motions," *Bulletin of the Seismological Society of America*, vol. 93, no. 3, pp. 1099–1131, 2003.
[31] L. Y. Lu, T. K. Lin, and S. W. Yeh, "Experiment and analysis of a leverage-type stiffness controllable isolation system for seismic engineering," *Earthquake Engineering & Structural Dynamics*, vol. 39, no. 15, pp. 1711–1736, 2010.
[32] S. Hochreiter and J. Schmidhuber, "Long short-term memory," *Neural Computation*, vol. 9, no. 8, pp. 1735–1780, 1997.
[33] Y. Bozorgnia, N. A. Abrahamson, L. A. Atik et al., "NGA-West2 research project," *Earthquake Spectra*, vol. 30, no. 3, pp. 973–987, 2014.
[34] S. K. Shahi and J. W. Baker, "An efficient algorithm to identify strong-velocity pulses in multicomponent ground motions," *Bulletin of the Seismological Society of America*, vol. 104, no. 5, pp. 2456–2466, 2014.
[35] T. Y. Hsu, S. K. Huang, Y. W. Chang et al., "Rapid on-site peak ground acceleration estimation based on supportvector regression and P-wave features in Taiwan," *Soil Dynamics and Earthquake Engineering*, vol. 49, pp. 210–217, 2013.
[36] C. J. Chen and T. K. Lin, "Development and application of a vibration isolation system with adaptive stiffness considering potential energy," *Sensors and Smart Structures Technologies for Civil, Mechanical, and Aerospace Systems*, vol. 9435, pp. 355–368, 2015.
[37] T. K. Lin, L. Y. Lu, C. E. Hsiao, and D. Y. Lee, "An intelligent semi-active solation system based on ground motion characteristic prediction," *Earthquakes and Structures*, vol. 22, no. 1, pp. 53–64, 2022.